Development and use of a ray-based analysis tool for the investigation of stimulated Raman scattering in laser-plasma interaction experiments

by

Steven Hironaka

A thesis submitted in partial fulfillment of the requirements for the degree of

Master of Science

in

Photonics and Plasmas

Department of Electrical and Computer Engineering
University of Alberta

Abstract

Recent long-scale-length spherical target experiments, performed on the OMEGA EP laser, are analyzed for stimulated Raman side-scattering (SRSS). This work has been motivated by results obtained on experiments performed at the National Ignition Facility (NIF), relevant to directly-driven inertial confinement fusion (ICF) [1, 2]. These NIF experiments have shown SRSS to be an important process, possibly responsible for the observed hot electron generation. Our model, based on ray tracing, is able to explain the time-dependent scattered light spectra from the OMEGA EP experiments: It identifies SRS side-scatter and near backscatter from portions of each incident beam where the scattered electromagnetic wave is generated in the direction parallel to contours of constant density. The nature of SRSS instability (temporal versus spatial growth) is discussed. It is suggested that the OMEGA EP platform could provide a good surrogate in which to develop SRSS mitigation strategies.

Preface

This thesis is an original work by Steven Hironaka. No part of this thesis has been previously published, except where noted:

- Chapter 5 contains "Identification of stimulated Raman side scattering in near-spherical coronal plasmas", S. Hironaka, J. Sivajeyan, M. J. Rosenberg, A. A. Solodov, T. Filkins, C. Z. Xiao, Q. Wang, and J. F. Myatt; to be submitted to Physics of Plasmas.

Acknowledgements

SH acknowledges the support of the Natural Sciences and Engineering Research Council of Canada (NSERC), [funding reference numbers RGPIN-2018-05787,RGPAS-2018-522497]. Cette recherche a été financée par le Conseil de recherches en sciences naturelles et en génie du Canada (CRSNG), [numéros de référence RGPIN-2018-05787, RGPAS-2018-522497].

Table of Contents

List of Figures

Chapter 1

Introduction

Fusion is a nuclear mechanism that releases a large amount of energy by combining two light atoms into a single heavier atom. The first achievable fusion mechanism (i.e, having the highest reaction cross-section) is that of a deuterium (D) atom (hydrogen with 1 neutron (n)) and a tritium (T) atom (hydrogen with 2 neutrons), this fusion mechanism is called DT fusion for short.

$$\mathrm{D} + \mathrm{T} \rightarrow \mathrm{He}^4(3.5\mathrm{MeV}) + \mathrm{n}(14.1\mathrm{MeV})$$

In this reaction the excess energy is carried by the (He^4) alpha particle (3.5 MeV) and a neutron (14.1 MeV). This energy can be thermalized and used to heat steam as in a conventional nuclear fission power plant. The reason this is the first achievable mechanism is because it has the lowest temperature and density requirements compared to using different fuel atoms. Currently there are two main approaches to creating controlled fusion conditions in laboratories. The first is magnetic confinement fusion (MCF) which uses magnetic fields to contain the fuel in a donut shaped "magnetic bottle" and then heat the fuel for a relatively long time, on the order of seconds. The other main approach to fusion is inertial confinement fusion (ICF). In this approach, lasers to are used to greatly compress and then heat the fuel to fusion conditions. The inertia (mass) of the target prevents disassembly of the fuel before the fusion reactions are complete[3]. This method requires a significantly higher density, or more compression, but for a much shorter period than MCF (eg., 10ns). In ICF, the DT

fuel is encapsulated in a sphere with an outer layer of CH called an ablator. The ablation layer is heated by the lasers and explodes outward which causes a counter force inwards (the ablation pressure) compressing the DT fuel.

There are two different approaches to ICF: one is indirect drive [4] and the other is direct drive [5]. Indirect drive uses an apparatus called a hohlrahm which is a cylinder of gold (or another heavy element) where the spherical fuel target is suspended inside (Fig 1.2). The lasers are directed towards the openings of the cylinder and hit the inner walls. The laser light interacts with the gold, heating the wall to such high temperatures (millions of K) that it emits x-rays. It is the x-rays inside of the hohlrahm which ablate and compress the target. The Lawerence Livermore National Laboratory (LLNL) is the leading laboratory conducting research in ICF using the National Ignition Facility (NIF) (Fig 1.3). It currently holds the record for the greatest fusion yield (at 1.3 MJ). The other main approach to ICF is direct drive which is where the lasers are directed right at the target itself (Fig 1.1).

1.1 Motivation

The potential of laser fusion is limited by laser plasma instabilities (LPI) that occur when intense laser light propagates through plasma. One of these limiting LPIs is stimulated Raman scattering (SRS) [6]. SRS is a resonant decay of the drive laser light into a lower frequency scattered light wave and a electron plasma wave (EPW). The electron plasma wave is an electrostatic wave that can accelerate electrons to high energy causing the fuel to be preheated. Preheating of the fuel lowers the compressibility of the fusion target. Since high densities are required to achieve ICF, compression is an important factor and limiting the amount of high energy electrons is essential. Raman scattering also introduces an energy loss in fusion experiments. The scattered light wave that results from SRS often leaves the plasma in such a way that is does not contribute to the compression. The lowest frequency that the scattered light can have is half of the frequency of the incident light [6], which means that half

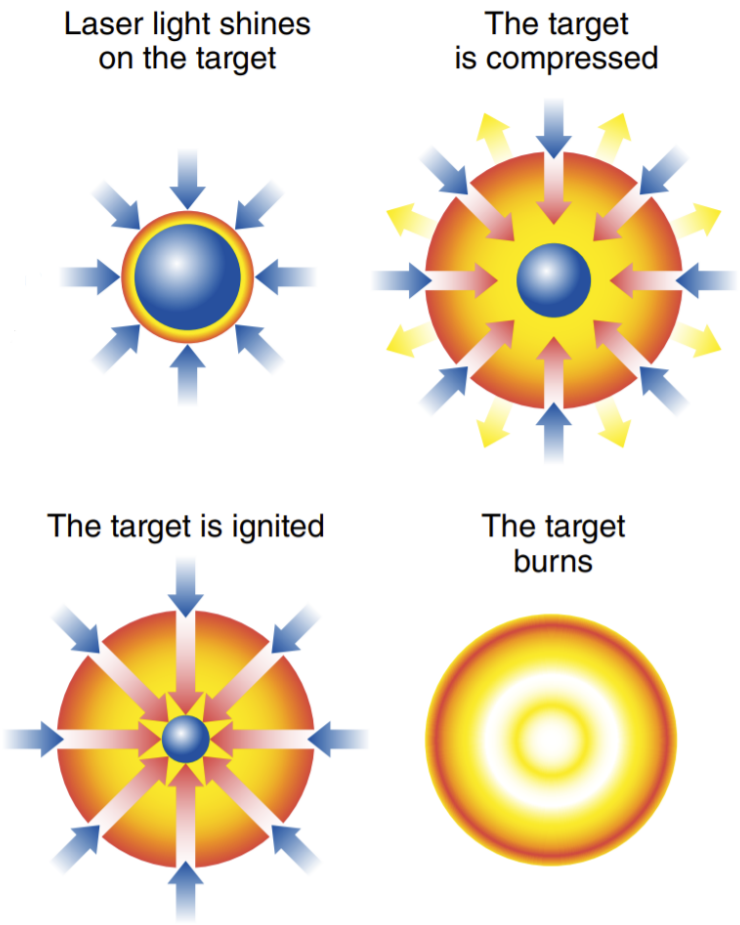

Figure 1.1: Shows the process of direct drive ICF. Lasers are shot at the target, the lasers heat the target and cause the outer ablation layer to explode. The ablation layer explodes outwards causing a counter force that compresses the fuel inside the target to densities where fusion can occur. Once fusion reactions begin, the energy that is released keeps the fuel hot enough for more reactions to occur. The blue arrows represent the laser light. The yellow arrows represent the explosion force of the outer ablation layer of the target. The red arrows represent the counter force from the explosion. This image was taken from Inertial Confinement Fusion: An Introduction published by the Laboratory for Laser Energetics at the University of Rochester.

or more than half of the energy in the incident light will be converted to scattered light and not used to heat the plasma. SRS is an issue in all laser fusion applications due to the inefficiency of energy transfer to the fuel, as well as the generation of high energy electrons which preheat the fuel. Finding the location and conditions where SRS occurs, and what causes it, is the first step to mitigating its deleterious effects in laser fusion.

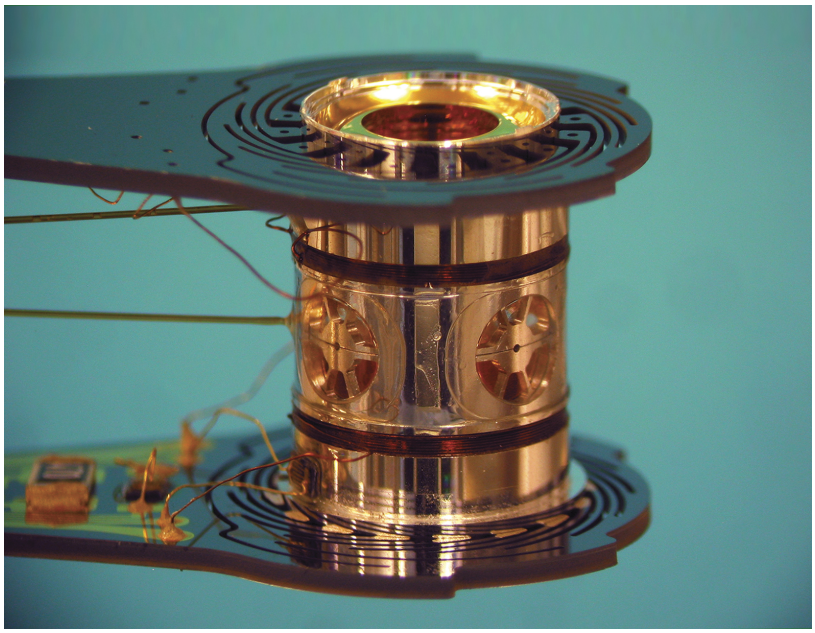

Figure 1.2: Shows a hohlrahm, which is the target apparatus used in indirect drive experiments. This image was taken from the photo gallery page of the Lawrence Livermore National Laboratory National Ignition Facility and Photon Science website: lasers.llnl.gov/media/photo-gallery.

Figure 1.3: Shows one of the two laser bays at the National Ignition Facility. These bays contain 96 each and are 122 meters (400 feet) long. This image was taken from the photo gallery page of the Lawrence Livermore National Laboratory National Ignition Facility and Photon Science website: lasers.llnl.gov/media/photo-gallery.

Laser fusion experiments performed with the OMEGA EP laser [7] at the Laboratory of Laser Energetics (LLE) at the University of Rochester have recently shown signatures of SRS detected by a scattered light diagnostic called the Sub-Aperture

Back-scatter Station (SABS). SABS measures the intensity of light that travels back towards one of the four drive lasers. We are able to simulate this experiment using numerical simulations of the target hydrodynamics and a ray tracing analysis that was developed as part of my thesis work. This ray tracing analysis used a new technique to find what SRS mechanisms contribute the most to the experimental detected results. The OMEGA EP fusion experiment that the research in this paper is based on is a two beam direct drive experiment with 700 μm diameter target sphere and 700 μm diameter laser focal spot.

As a final motivational note: on August 8, 2021 while preparing this thesis, there was a indirect drive shot (shot 210808) at the National Ignition Facility (NIF) that resulted in 1.3 MJ of fusion energy. This shot shows a large improvement over previous shots done at NIF in both fusion yield, by a factor of $\sim$8, and hot spot temperature, by a factor of $\sim$2 in keV. This large improvement can be attributed to burn propagation. Burn propagation is where the alpha particles (helium ions) that are created from the fusion reactions keep the fuel plasma hot enough for more reactions to occur after the laser pulses have finished. In previous experiments, the peak density and peak neutron yield have occurred at the same time. In this high yield shot, the peak neutron yield occurred after the peak density had occurred, which is evidence of burn propagation.

1.2 Thesis Objectives

The purpose of this research is to identify the parameters of SRS mechanisms that result in a high gain detected by the diagnostics. From experimental data, we have the intensity of detected Raman light with respect to the wavelength of the light over the duration of the experiment. With the ray tracing, we can simulate the experiment and look at which SRS rays have the largest gains and would contribute the most to the detected SRS. After finding these high gain rays, we can look at what portion of the incident beams the Raman light is coming from and what angle the Raman

light launches at. Knowing where the high gain Raman comes from and what angle it launches at can help in designing future fusion experiments to mitigate SRS.

1.3 Thesis Outline

This thesis is organized as follows: Chapter 2 describes the physics of the stimulated Raman scattering instability.; Chapter 3 describes the ray tracing of electromagnetic and electron plasma waves.; Chapter 4 describes how the MATLAB code created through my thesis work predicts the scattered light spectra of the OMEGA EP diagnostic.; Chapter 5 describes the applications of the MATLAB code to investigate SRS in recent experiments.; Finally, Chapter 6 presents a summary and conclusions.

References

[3] J. Nuckolls, L. Wood, and A. Thiessen, "Laser compression of matter to super-high densities: Thermonuclear (ctr) applications," vol. 239, 1972. DOI: 10.1038/239139a0.

[4] J. Lindl, "Development of indirect-drive approach to inertial confinement fusion and the target physics basis for ignition and gain," *Physics of Plasmas*, vol. 2, 1995. DOI: 10.1063/1.871025.

[5] R. S. Craxton, K. S. Anderson, T. R. Boehly, V. N. Goncharov, D. R. Harding, J. P. Knauer, R. L. McCrory, P. W. McKenty, D. D. Meyerhofer, J. F. Myatt, A. J. Schmitt, J. D. Sethian, R. W. Short, S. Skupsky, W. Theobald, W. L. Kruer, K. Tanaka, R. Betti, T. J. B. Collins, J. A. Delettrez, S. X. Hu, J. A. Marozas, A. V. Maximov, D. T. Michel, P. B. Radha, S. P. Regan, T. C. Sangster, W. Seka, A. A. Solodov, J. M. Soures, C. Stoeckl, and J. D. Zuegel, "Direct-drive inertial confinement fusion: A review," *Phys. Plasmas*, vol. 22, no. 11, p. 110 501, 2015. DOI: 10.1063/1.4934714.

[6] W. L. Kruer, "The Physics of Laser Plasma Interactions," in, ser. Frontiers in Physics, D. Pines (Ed.) Vol. 73, Redwood City, CA: Addison-Wesley, 1988.

[7] M. J. Rosenberg, A. A. Solodov, J. F. Myatt, S. Hironaka, R. K. Follett, T. Filkins, A. V. Maximov, C. Ren, S. Cao, P. Michel, W. Seka, M. S. Wei, M. Hohenberger, J. P. Palastro, R. H. H. Scott, K. Glize, and S. P. Regan, "Effect of overlapping laser beams and density scale length in laser-plasma instability experiments on omega ep (**in preparation**)," *Phys. Plasmas*, 2021.

Chapter 2

Stimulated Raman Scattering

Two of the main instabilities that are concerning for laser fusion experiments are resonant three wave coupling instabilities [6]. These three wave coupling instabilities arise when a large amplitude incident light wave is coupled with a scattered light wave and, either an electron plasma (Langmuir) wave for the Raman instability or an ion acoustic wave for the Brillouin instability. The names of these instabilities are borrowed from similar scattering mechanisms that exist in nonlinear optics of solids [8]. The reason these are instabilities in the case of laser fusion is because the incident light is extremely intense ($\geq 10^{15}$ W/cm^2). The stimulated Raman scattering instability caused lots of problems in the 2011 ignition campaign when the NIF-the world's most energetic laser-became operational. Hundreds of kJs of Raman light was observed in the National Ignition Campaign [9]. This electron plasma wave can have a very high phase velocity (of order the velocity of light) and so can produce very energetic electrons when it damps. These highly energetic electrons can preheat the fuel in laser fusion applications. When the fuel is preheated, it is harder to compress and lowers the peak density of a shot. This preheating issue is why the Raman instability is a particularly significant concern for laser fusion.

The Raman instability can be simply described as an incident photon depositing some of its energy into the plasma as an electron plasma wave (or plasmon) and the remainder in a scattered photon. The frequency and wave number matching

conditions for the Raman instability are

$$\omega_0 = \omega_s + \omega_{EPW}, \tag{2.1}$$

$$\mathbf{k}_0 = \mathbf{k}_s + \mathbf{k}_{EPW}. \tag{2.2}$$

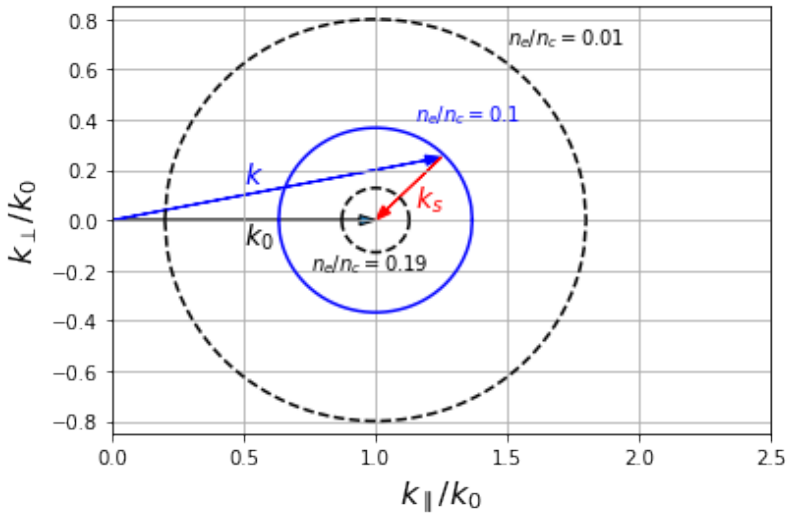

Figure 2.1: The wave number matching conditions.

where ω_0 (ω_s) and $\mathbf{k}_0$ ($\mathbf{k}_s$) are the frequency and wave number of the incident (scattered) light wave, and ω_{EPW} ($\mathbf{k}_{EPW}$) is the frequency (wavenumber) of the electron plasma wave. The wave number matching conditions are illustrated in Fig. 2.1. The instability requires that $\omega_0 \gtrsim 2\omega_{pe}$, where $\omega_{pe} = 4\pi e^2 n_e/m_e$ is the electron plasma frequency, n_e, m_e are the electron number density and mass, respectively, while e is the elementary charge. This is because the dispersion relation of both the scattered light wave and electron plasma waves must be satisfied and both require the frequency of the waves to be greater than ω_{pe}.

The reason the frequency of a light wave needs to be greater than ω_{pe} to propagate in a plasma is that the maximum frequency of the electron current is ω_{pe}. For EM waves with frequencies lower than this, the electron current cancels the displacement current that is required for EM wave propagation.

In the process of the Raman instability, part of the incident energy is scattered in the form of a red-shifted light wave, and part is deposited into an electron plasma wave. By multiplying the frequency matching condition [Eq. (2.1)] by $\hbar$ (Planck's constant) and noting that $\hbar\omega$ is the energy of a photon or plasmon, it can be seen that for each photon undergoing this process, the fraction of its energy transferred to the plasma wave is $(\omega_{\mathrm{EPW}}/\omega_0)$. This portion of the energy will heat the plasma as the electron plasma wave damps as it propagates through the plasma.

The Raman instability has a feedback loop that is responsible for the instability (Fig. 2.2). Before giving a mathematical derivation, it is imperative to first consider the physical mechanisms that are at play: Consider an incident pump light wave with electric field amplitude $\mathbf{E}_L$ propagating through a plasma with a density fluctuation (δn) along the direction of propagation, that is associated with an electron plasma wave. Since the electrons oscillate in the light wave with the velocity

$$\mathbf{v}_{os} = \frac{e\mathbf{E}_L}{m_e\omega_0}, \tag{2.3}$$

a transverse current $\delta\mathbf{J} = -e\mathbf{v}_{os}\delta n$ is generated.

This transverse current generates a scattered light wave with an amplitude $\delta\mathbf{E}$ which interferes with the incident light to produce a variation in the wave pressure

$$\nabla(E^2/8\pi) = \nabla(\mathbf{E}_L \cdot \delta\mathbf{E})/4\pi. \tag{2.4}$$

Variations in wave pressure push plasma from regions of high pressure to regions of low pressure and vice versa. A density fluctuation is generated which reinforces the original perturbation if the wave numbers are suitably matched [Eqs. (2.1) & (2.2)]. Due to this feed-back loop, an instability is possible: A small density fluctuation leads to a transverse current which generates a small scattered light wave, which can in turn reinforce the density fluctuation via a variation in the wave pressure.

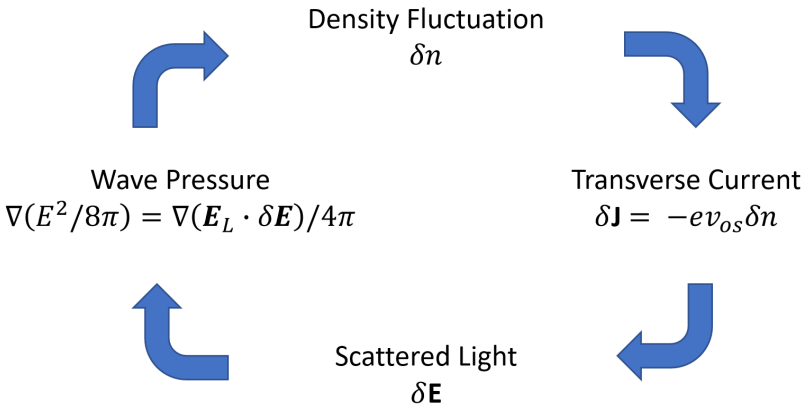

Figure 2.2: A visual representation of the Raman instability feedback loop.

2.1 Instability analysis

The coupled equations describing the Raman instability can be derived starting from Maxwell's equations and a fluid model for the electron response. For this derivation, consider a light wave propagating through a plasma which is spatially uniform in density and temperature. It is particularly convenient to use the electric and magnetic fields in terms of the vector potential $\mathbf{A}$ and the electrostatic potential ϕ, where $\mathbf{B} = \nabla \times \mathbf{A}$ and $\mathbf{E} = -\nabla\phi - c^{-1}\partial\mathbf{A}/\partial t$. Starting with the Ampere-Maxwell equation

$$\nabla \times \mathbf{B} = \frac{4\pi}{c}\mathbf{J} + \frac{1}{c}\frac{\partial \mathbf{E}}{\partial t}, \tag{2.5}$$

substituting for $\mathbf{E}$ and $\mathbf{B}$, and choosing the Coulomb gauge, $\nabla \cdot \mathbf{A} = 0$, we obtain the wave equation for $\mathbf{A}$ in terms of the plasma current and electrostatic potential:

$$\left(\frac{1}{c^2}\frac{\partial^2}{\partial t^2} - \nabla^2\right)\mathbf{A} = \frac{4\pi}{c}\mathbf{J} - \frac{1}{c}\frac{\partial}{\partial t}\nabla\phi.$$

The current density $\mathbf{J}$ naturally splits into its transverse part $\mathbf{J}_\mathrm{t}$ (transverse in relation to the light wave k-vectors) and its longitudinal part $\mathbf{J}_l$ (which is related to the electrostatic plasma wave). The longitudinal part of $\mathbf{J}$ is related to $\nabla\phi$ via Poisson's equation and the equation for conservation of charge (obtained by taking the divergence of Eq. (2.5) and making use of Poisson's equation):

$$\nabla^2\phi = -4\pi\rho \tag{2.6}$$

$$\frac{\partial\rho}{\partial t} + \nabla\cdot\mathbf{J} = 0, \tag{2.7}$$

where ρ is the charge density. Taking the time derivative of Eq. (2.6) and substituting for $\partial\rho/\partial t$ gives

$$\nabla\cdot\left(\frac{\partial}{\partial t}\nabla\phi - 4\pi\mathbf{J}\right) = 0. \tag{2.8}$$

Since $\nabla\cdot\mathbf{J}_\mathrm{t} = 0$ by definition, we obtain:

$$\frac{\partial}{\partial t}\nabla\phi = 4\pi\mathbf{J}_l. \tag{2.9}$$

Hence we arrive at a wave equation for the vector potential $\mathbf{A}$ with a source term that is proportional to the transverse current:

$$\left(\frac{1}{c^2}\frac{\partial^2}{\partial t^2} - \nabla^2\right)\mathbf{A} = \frac{4\pi}{c}\mathbf{J}_\mathrm{t}. \tag{2.10}$$

Assuming the EM wave is polarized such that its electric field vector (polarization) has no component in the direction of variation of the electron density ($\mathbf{A}\cdot\nabla n_\mathrm{e} = 0$), the transverse current can be expressed as $\mathbf{J}_\mathrm{t} = -n_\mathrm{e}e\mathbf{u}_\mathrm{t}$. Where $\mathbf{u}_\mathrm{t}$ is the oscillation velocity of an electron in the electric field of the light wave and n_e is the electron density. For $|\mathbf{u}_\mathrm{t}| \ll c$ which is typical for ICF conditions, $\mathbf{u}_\mathrm{t} = e\mathbf{A}/m_e c$ since

$$\frac{\partial\mathbf{u}_\mathrm{t}}{\partial t} = -\frac{e}{m_e}\mathbf{E}_\mathrm{t} = \frac{e}{m_e c}\frac{\partial\mathbf{A}}{\partial t}. \tag{2.11}$$

Hence, we obtain an equation for the propagation of a light wave in a plasma:

$$\left(\frac{\partial^2}{\partial \mathrm{t}^2} - c^2\nabla^2\right)\mathbf{A} = -\frac{4\pi e^2}{m_e}n_\mathrm{e}\mathbf{A}. \tag{2.12}$$

The scattering of a large amplitude light wave ($\mathbf{A}_L$) by a small amplitude density fluctuation ($\tilde{n}_\mathrm{e}$) about n_0 (the uniform background plasma density), can be determined by substituting for $\mathbf{A} = \mathbf{A}_L + \tilde{\mathbf{A}}$ and for $n = n_0 + \tilde{n}_\mathrm{e}$ in Eq. (2.12). Linearization leads to an equation for the scattered light wave $\tilde{\mathbf{A}}$

$$\left(\frac{\partial^2}{\partial \mathrm{t}^2} - c^2\nabla^2 + \omega_{\mathrm{pe}}^2\right)\tilde{\mathbf{A}} = -\frac{4\pi e^2}{m_e}\tilde{n}_\mathrm{e}\mathbf{A}_L. \tag{2.13}$$

As in our earlier heuristic description, the right hand side is the transverse current ($\alpha\ \tilde{n}_\mathrm{e}\mathbf{v}_{os}$) which produces the scattered light wave ($\tilde{\mathbf{A}}$).

To derive an equation for the density fluctuation associated with the electron plasma wave $\tilde{n_e}$, it is possible to treat the ions as a fixed, neutralizing, background since they have too much inertia to react to electric fields of frequencies as high as ω_{pe}. The electrons as a warm fluid. The continuity and force equations comprising this model are:

$$\frac{\partial n_\mathrm{e}}{\partial t} + \nabla\cdot(n_\mathrm{e}\mathbf{u}_\mathrm{e}) = 0 \tag{2.14}$$

$$\frac{\partial \mathbf{u}_\mathrm{e}}{\partial \mathrm{t}} + \mathbf{u}_\mathrm{e}\cdot\nabla\mathbf{u}_\mathrm{e} = -\frac{e}{m_e}\left(\mathbf{E} + \frac{\mathbf{u}_\mathrm{e}\times\mathbf{B}}{c}\right) - \frac{\nabla p_\mathrm{e}}{n_\mathrm{e}m_e}, \tag{2.15}$$

where n_e, $\mathbf{u}_\mathrm{e}$ and p_e are the density, velocity and pressure of the electron fluid, respectively. Separating the velocity into longitudinal ($\mathbf{u_L}$) and transverse components ($\mathrm{e}\mathbf{A}/m_e c$) ($\mathbf{u}_\mathrm{e} = \mathbf{u}_L + e\mathbf{A}/m_e c$), substituting into the above momentum equation, and using a standard vector identity gives an equation for $\mathbf{u}_L$:

$$\frac{\partial \mathbf{u}_L}{\partial \mathrm{t}} = \frac{e}{m_e}\nabla\phi - \frac{1}{2}\nabla\left(\mathbf{u}_L + \frac{e\mathbf{A}}{m_e c}\right)^2 - \frac{\nabla p_\mathrm{e}}{n_\mathrm{e}m_e}. \tag{2.16}$$

The second term on the right hand side is the ponderomotive force (related to the gradient of the wave pressure mentioned earlier) and is proportional to the gradient of the intensity of both the longitudinal and transverse components of the electric field.

We now use the adiabatic equation of state ($p_{\rm e}/n_{\rm e}^3$ = constant) in order to unite the plasma pressure in terms of density and linearize the continuity and momentum equations. In particular, we take $\mathbf{u}_L = \tilde{\mathbf{u}}$, $n_{\rm e} = n_0 + \tilde{n}_{\rm e}$, $\mathbf{A} = \mathbf{A}_L + \tilde{\mathbf{A}}$ and $\phi = \tilde{\phi}$ where the tilde denotes an infinitesimal quantity. The linearized electron fluid equations become:

$$\frac{\partial \tilde{n}_{\rm e}}{\partial t} + n_0 \nabla \cdot \tilde{\mathbf{u}} = 0, \tag{2.17}$$

$$\frac{\partial \tilde{\mathbf{u}}}{\partial t} = \frac{e}{m_e}\nabla\tilde{\phi} - \frac{e^2}{m_e^2 c^2}\nabla(\mathbf{A}_L \cdot \tilde{\mathbf{A}}) - \frac{3v_{\rm Te}^2}{n_0}\nabla\tilde{n}_{\rm e}, \tag{2.18}$$

where $v_{\rm Te} = \sqrt{T_e/m_e}$ is the electron thermal velocity. Taking a time derivative of the continuity, then a divergence of the momentum equation, and finally eliminating the term $\partial(\nabla \cdot \tilde{\mathbf{u}}_{\mathbf{L}})/\partial \mathbf{t}$ gives our equation for the electron density perturbation that is reinforced by the wave pressure (LHS term):

$$\left(\frac{\partial^2}{\partial t^2} + \omega_{\rm pe}^2 - 3v_{\rm Te}^2\nabla^2\right)\tilde{n}_{\rm e} = \frac{n_0 e^2}{m_e^2 c^2}\nabla^2(\mathbf{A}_L \cdot \tilde{\mathbf{A}}). \tag{2.19}$$

This equation describes the generation of a density fluctuation caused by the beating/interference between the large amplitude EM wave ($\mathbf{A}_L$) and the scattered wave ($\tilde{\mathbf{A}}$).

2.2 Dispersion relation

Eqs. (2.13) and (2.19) above describe the coupling of the electrostatic and electromagnetic waves discussed in the introduction of this chapter. To derive the dispersion relation for the Raman instability and to see how the wave number/frequency matching conditions arise, we take $\mathbf{A}_L = \mathbf{A}_0 \cos(\mathbf{k}_0 \cdot \mathbf{x} - \omega_0 t)$ and Fourier analyze these equations. The result is:

$$(\omega^2 - k^2c^2 - \omega_{\rm pe}^2)\tilde{\mathbf{A}}(\mathbf{k},\omega) =$$
$$\frac{4\pi e^2}{2m_e}\mathbf{A}_0\left[\tilde{n}_{\rm e}(k-k_0,\omega-\omega_0)+\tilde{n}_{\rm e}(k+k_0,\omega+\omega_0)\right], \tag{2.20}$$
$$(\omega^2 - \omega_{\rm EPW}^2)\tilde{n}_{\rm e}(\mathbf{k},\omega) =$$
$$\frac{k^2e^2n_0}{2m_e^2c^2}\mathbf{A}_0\cdot\left[\tilde{\mathbf{A}}(\mathbf{k}-\mathbf{k_0},\omega-\omega_\mathbf{0})+\tilde{\mathbf{A}}(\mathbf{k}+\mathbf{k_0},\omega+\omega_\mathbf{0})\right], \tag{2.21}$$

where $\omega_{\rm EPW} = (\omega_{\rm pe}^2 + 3k_{\rm EPW}^2 v_{\rm Te}^2)^{1/2}$ is the Bohm-Gross frequency, ω_0 and k_0 are the frequency and wave number of the large amplitude light wave, and ω and $\mathbf{k}$ are the Laplace and Fourier variables, respectively. We next use the first equation [Eq. (2.20)] to eliminate $\tilde{\mathbf{A}}$ from the second [Eq. (2.21)] and assuming polarization is perpendicular to the scattering plane. Taking $\omega \simeq \omega_{\rm pe}$, such that ω corresponds very closely with the EPW frequencies, and neglecting the terms $\tilde{n}_{\rm e}(k-2k_0,\omega-2\omega_0)$ and $\tilde{n}_{\rm e}(k+2k_0,\omega+2\omega_0)$ as very non-resonant, we obtain the dispersion relation:

$$\omega^2 - \omega_{\rm EPW}^2 = \frac{\omega_{\rm pe}^2 k^2 v_{\rm os}^2}{4}\left[\frac{1}{D(\omega-\omega_0,\mathbf{k}-\mathbf{k}_0)} + \frac{1}{D(\omega+\omega_0,\mathbf{k}+\mathbf{k}_0)}\right]. \tag{2.22}$$

Here $D_t(\omega,k) = \omega^2 - k^2c^2 - \omega_{\rm pe}^2$ is the dispersion function for EM waves in plasma and $v_{\rm os}$ is the oscillatory velocity of an electron in the large amplitude light wave. [A useful engineering formula is: $v_{\rm os} = 8.095\times10^8\sqrt{I_{15}}\lambda_{0,\mu\rm m}$ cm/sec, where $\lambda_{0,\mu\rm m}$ is the laser wavelength in microns, and $\sqrt{I_{15}}$ is the laser wavelength in units of 10^{15} W/cm^2.]

The instability growth rates can be found from the dispersion relation given in Eq. (2.22). For back or sidescatter (relative to k_0), we can neglect the upshifted (anti-stokes) light wave as non-resonant $D(\omega+\omega_0,\mathbf{k}+\mathbf{k}_0) \gg 1$, giving:

$$(\omega^2 - \omega_{\rm EPW}^2)[(\omega-\omega_0)^2 - (\mathbf{k}-\mathbf{k}_0)^2c^2 - \omega_{\rm pe}^2] = \frac{\omega_{\rm pe}^2 k^2 v_{\rm os}^2}{4}.$$

Or, on introducing the dispersion function for the plasma waves $D_l(\omega,k) \equiv \omega^2 - \omega_{\rm EPW}^2(\mathbf{k})$:

$$D_l(\omega, \mathbf{k}) D_t(\omega - \omega_0, \mathbf{k} - \mathbf{k}_0) = \frac{\omega_{\rm pe}^2 k^2 v_{\rm os}^2}{4}, \tag{2.23}$$

where the subscripts l and t distinguish the dispersion functions for the longitudinal (plasma wave) and transverse (EM) waves, respectively. From the above dispersion relation, we can see why the instability is of the three-wave coupling type: The EPW (D_l) is coupled to a scattered EM wave (D_t) by the large amplitude wave ($v_{\rm osc}^2$). We take $\omega = \omega_{\rm EPW} + \delta\omega$ to be nearly resonant, where $\delta\omega \ll \omega_{\rm EPW}$, and note that maximum growth occurs when the (frequency-downshifted/Stokes) scattered light wave is also resonant i.e., when

$$(\omega_{\rm EPW} - \omega_0)^2 - (\mathbf{k} - \mathbf{k}_0)^2 c^2 - \omega_{\rm pe}^2 = 0. \tag{2.24}$$

We then use the envelope approximation (which assumes $\delta\omega \ll \omega_{\rm EPW}$):

$$D_l(\omega_{\rm EPW} + \delta\omega, \mathbf{k}) \simeq \frac{\partial D_l}{\partial \omega_{\rm EPW}} \delta\omega = 2\omega_{\rm EPW}\, \delta\omega, \tag{2.25}$$

$$D_t(\omega_{\rm EPW} - \omega_0 + \delta\omega, \mathbf{k} - \mathbf{k}_0) = \frac{\partial D_t}{\partial(\omega_{\rm EPW} - \omega_0)} \delta\omega = 2(\omega_{\rm EPW} - \omega_0)\, \delta\omega. \tag{2.26}$$

On substitution of Eqs. (2.25) and (2.26) into Eq. (2.23) we obtain:

$$4\, \omega_{\rm EPW}(\omega_{\rm EPW} - \omega_0)\, \delta\omega^2 = \frac{\omega_{\rm pe}^2 k^2 v_{\rm os}^2}{4} \tag{2.27}$$

$$\delta\omega^2 = -\frac{k^2 v_{\rm os}^2}{16} \frac{\omega_{\rm pe}^2}{\omega_{\rm EPW}(\omega_0 - \omega_{\rm EPW})}. \tag{2.28}$$

From Eq. (2.28) we see that the correction to the EPW frequency is purely imaginary ($\delta\omega = i\gamma$). An imaginary frequency corresponds to exponential growth in time $e^{\gamma t}$. The solution for γ is:

$$\gamma = \frac{k v_{\rm os}}{4} \left[\frac{\omega_{\rm pe}^2}{\omega_{\rm EPW}(\omega_0 - \omega_{\rm EPW})} \right]^{1/2}. \tag{2.29}$$

The wave number k is determined by the condition that the EM wave is also resonant [Eq.(2.24)]. For example, for direct backscatter where the growth rate maximizes (k is largest), we have:

$$k = k_0 + \frac{\omega_0}{c}\left(1 - \frac{2\omega_{\rm pe}}{\omega_0}\right)^{1/2}. \tag{2.30}$$

The wave number $\mathbf{k}$ of the EPW depends on the electron plasma density where the instability occurs (Fig. 2.3), it starts from $k = 2k_0$ for $n \ll n_{\rm c}/4$, and goes to $k = k_0$ for $n \sim n_{\rm c}/4$, as is apparent from the matching condition.

Note that we can write the resonance condition [Eq. (2.30)] as

$$(\mathbf{k} - \mathbf{k}_0)^2 = k_0^2\left[1 - 2\left(\frac{n_{\rm e}}{n_{\rm c}}\right)^{1/2}\left(1 + \frac{3}{2}k^2\lambda_{\rm De}^2\left[1 - \left(\frac{n_{\rm e}}{n_{\rm c}}\right)^{1/2}\right]\right)\right], \tag{2.31}$$

which can be approximated as

$$(\mathbf{k} - \mathbf{k}_0)^2 = k_0^2\left[1 - 2\left(\frac{n_{\rm e}}{n_{\rm c}}\right)^{1/2}\right], \tag{2.32}$$

since $k^2\lambda_{\rm D}^2 \ll 1$ for parameters relevant to ICF.

The wave number and growth rate are less for any 90° sidescatter ($k \simeq \sqrt{2}k_0$ for $n \ll n_{\rm c}/4$) compared to backscatter (recall that directions are given relative to $\mathbf{k}_0$). For the more general case of sidescatter in which $\mathbf{A} \cdot \nabla n \neq 0$, the growth rate is further reduced since the electric vectors of the incident and scattered light waves are no longer aligned. For example, it is apparent from the equation for $\tilde{n}_{\rm e}$ [Eq. (2.21)], from the start of this section, that the growth rate will vanish when $\tilde{\mathbf{A}} \cdot \mathbf{A_0} = \mathbf{0}$. Hence sidescatter occurs preferentially out of the plane of polarization, the case we have treated.

[We remark on an important point here that must be understood: The terminology of "sidescatter" can be confusing because it can refer to two different processes: (1) is

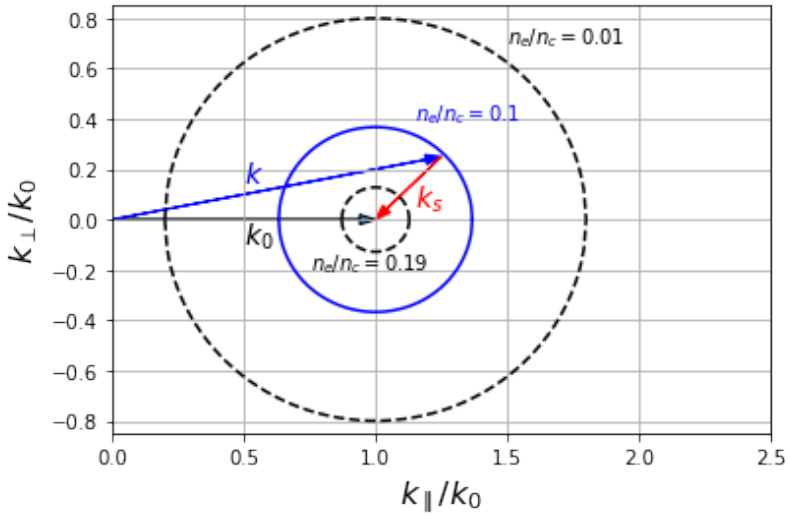

Figure 2.3: The wave number matching conditions for SRS, showing the dependence on density [Eq.(2.32)].

sidescatter relative to the direction of the pump - as described here - or (2) sidescatter relative to the direction of the density gradient. It is the latter that is described in Chapter 5 and is of the most interest).]

Finally, note that for forward scatter at very low densities, $k \ll \omega_0/c$, both the upshifted and downshifted light waves can now be nearly resonant i.e.,

$$D(\omega \pm \omega_0, \mathbf{k} \pm \mathbf{k}_0) \simeq 2(\omega_{\rm pe} \pm \omega_0)\delta\omega,$$

choosing $k = \omega_{\rm pe}/c$ and let $\omega = \omega_{\rm pe} + \delta\omega$, where $\delta\omega \ll \omega_{\rm pe}$. Substituting into the dispersion relation, we find the maximum growth rate ($\delta\omega = i\gamma$):

$$\gamma \simeq \frac{\omega_{\rm pe}^2}{2\sqrt{2}\omega_0}\frac{v_{\rm os}}{c}. \tag{2.33}$$

2.3 Threshold due to wave damping

Equation (2.29) implies that even an infinitesimally small incident light wave will lead to instability and exponential growth of the decay waves in time. In practice, some threshold intensity is required. To introduce the concept we introduce damping

and see that such damping of the unstable waves introduces a threshold intensity for instability generation. The simplest way to include the effect of damping is to add the phenomenological terms $\nu_{\rm s}(\partial\tilde{\mathbf{A}}/\partial\mathbf{t})$ and $\nu_{\rm e}(\partial\tilde{n}/\partial t)$ to Eqs. (2.25) and (2.26) in Section 2.2, where $\nu_{\rm s}$ ($\nu_{\rm e}$) is the energy damping rate for the scattered light wave (the electron plasma wave). The dispersion relation [Eq. (2.22)] remains the same as before with the substitutions:

$$\omega^2 - \omega_{\rm pe}^2 \rightarrow \omega(\omega + i\nu_{\rm e}) - \omega_{\rm pe}^2, \quad \text{and} \quad D(\omega,k) \rightarrow \omega(\omega + i\nu_{\rm s}) - k^2c^2 - \omega_{\rm pe}^2.$$

With this substitution, the instability analysis proceeds as before. For example, for back or sidescatter, we again retain only the down-shifted light wave, take $\omega = \omega_{\rm EPW} + i\gamma$, and choose k according to the resonance condition to obtain maximum growth. Then we obtain

$$(\gamma + \gamma_{\rm e})(\gamma + \gamma_{\rm s}) = \gamma_0^2, \tag{2.34}$$

where $\gamma_{\rm e}$ and $\gamma_{\rm s}$ are the amplitude damping rates (half of the energy damping rates ν_e and ν_s) and γ_0 is the growth rate in the absence of damping [Eq. (2.34)]. The threshold condition due to damping then is

$$\gamma_0 \geq \sqrt{\gamma_{\rm e}\gamma_{\rm s}}. \tag{2.35}$$

As an example, we consider backscatter for $\omega_{\rm pe}/\omega_0 \ll 1/2$ and assume only collisional damping ν_e. Substituting the expression for the growth rate into the above then gives the threshold condition:

$$\left(\frac{v_{\rm os}}{c}\right)^2 > \left(\frac{\omega_{\rm pe}}{\omega_0}\right)^2 \frac{\nu_{\rm ei}^2}{\omega_0\omega_{\rm pe}},$$

where $\nu_{\rm ei}$ is the collision frequency. This threshold intensity can be quite low in fact it is almost always exceeded in ICF experiments; In general, Landau damping of the

plasma wave needs to be included. This result is useful, however, as it permits an intuitive description to be obtained for the main physical process responsible for the SRS threshold in ICF.

2.4 Threshold due to plasma inhomogeneity

In practice, gradients in the plasma density have much more influence on the threshold intensity ($v_{\rm osc}$) compared to damping. To see this, remember that the resonance conditions must be fulfilled for there to be an instability:

$$\omega_0 = \omega_{\rm s} + \omega_{\rm EPW},$$
$$\mathbf{k}_0 = \mathbf{k}_{\rm s} + \mathbf{k}_{\rm EPW}.$$

When considering an inhomogeneous plasma, [i.e., one where the plasma density and temperature vary in space] the wave numbers become functions of position. This means that, if the resonance conditions are satisfied at some z=0, a mismatch κ will be present at other locations:

$$\kappa = k_0(z) - k_s(z) - k_{\rm EPW}(z).$$

We can estimate how far in z we have to move resonance from the point $\kappa(z=0)=0$ before resonant interaction is lost. To do this, we (somewhat arbitrarily) require that the resonance will be lost when the accumulated mismatch in phase is one-half:

$$\int_0^{l_{\rm INT}} \kappa \, {\rm d}z \sim 1/2,$$

where $l_{\rm INT}$ represents the size of the resulting interaction region. [This is a 1-D approach, where the z direction is the direction in which the plasma variables are changing. This means that the wave numbers in the above expression for κ are the components in this direction.] Taylor expanding about the matching point [($\kappa = \kappa(0) + \kappa' z$)] gives, by elementary integration, the resonance length:

$$l_{\mathrm{INT}} \sim 1/\sqrt{\kappa'}.$$

We make the connection with the previous damping threshold by noting that the decay waves dissipate some of their energy when propagating out of the interaction region. In this way, we introduce an "effective damping rate" that is approximately given by:

$$\nu_{\mathrm{eff}} \equiv v_{\mathrm{g}i}/l_{\mathrm{INT}},$$

where $v_{\mathrm{g}i}$ is the component of the group velocity of the i^{th} wave (i = s, EPW) along the gradient (i.e., in the z direction). Inserting these effective damping rates into Eq. (2.35) for the threshold that was computed using real damping gives:

$$\frac{\gamma_0^2}{|\kappa' v_{\mathrm{gs}} v_{\mathrm{gEPW}}|} \gtrsim 1. \tag{2.36}$$

Somewhat fortuitously, this is the (correct) result obtained by a detailed analysis, however, there is a caveat: spatial inhomogeneity converts the instability from one that grows in time to one that grows in space. The threshold condition given by Eq. (2.36) is the condition for $\exp(2\pi)$ spatial growth in intensity. More generally, the expression for the spatial amplification in intensity is:

$$I = I_0 \exp\left[\frac{2\pi\gamma_0^2}{|\kappa' v_{\mathrm{gs}} v_{\mathrm{gEPW}}|}\right],$$

where the (gain) factor in the exponent is known as the "Rosenbluth gain":

$$G = \frac{2\pi\gamma_0^2}{|\kappa' v_{\mathrm{gs}} v_{\mathrm{gEPW}}|}. \tag{2.37}$$

Recall that we have previously defined γ_0:

$$\gamma_0 = \frac{k v_{\mathrm{os}}}{4}\left[\frac{\omega_{\mathrm{pe}}^2}{\omega_{\mathrm{EPW}}(\omega_0 - \omega_{\mathrm{EPW}})}\right]^{1/2}.$$

Since we will make use of it later, we consider Raman backscatter at $n \ll n_c/4$ and compile both the threshold and the Rosenbluth gain.

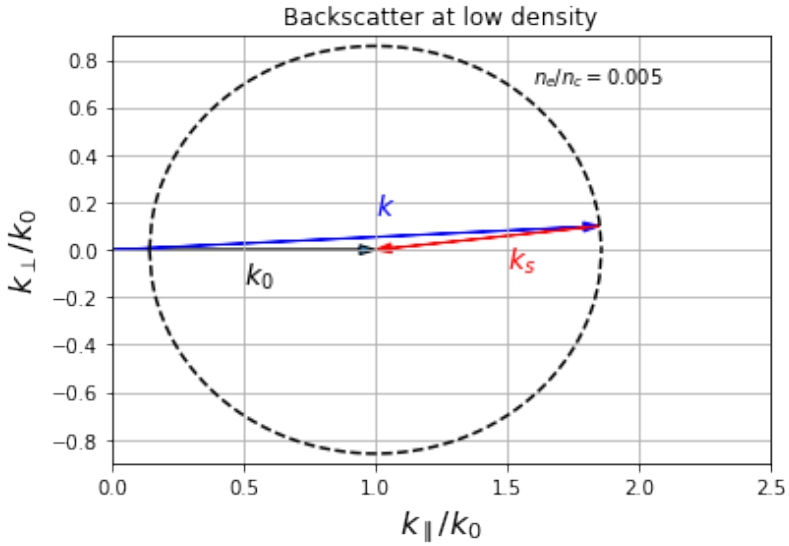

Figure 2.4: Wave vector diagram for near SRS backscatter at small plasma densities.

The calculation is simplified since the wave number of the electron plasma wave depends more sensitively on density than the wave numbers of the transverse waves do. We can then make the approximation

$$\kappa' \simeq -\partial k/\partial z,$$

and hence

$$|v_{\mathrm{g,EPW}}\kappa'| \sim \partial\omega_{\mathrm{pe}}/\partial z.$$

Neglecting temperature gradients and assuming a locally linear variation in density with a scale length $L = n_e/(\partial n_e/\partial z)$, we find that $\partial\omega_{\mathrm{pe}}/\partial z \simeq \omega_{\mathrm{pe}}/(2L)$. Noting that $v_{\mathrm{gs}} \simeq c$ and substituting into the Rosenbluth expression [Eq. (2.36)], we obtain the threshold condition:

$$\left(\frac{v_{\mathrm{os}}}{c}\right)^2 > \frac{2}{k_0 L},$$

and the Rosenbluth gain:

$$G = \pi k_0 L(\frac{v_{\rm osc}}{c})^2. \tag{2.38}$$

The Rosenbluth gain has been the standard formula used for evaluating the gain of stimulated Raman scattering in laser fusion experiments. The major flaw in using the Rosenbluth gain formula is that it diverges when the scattering angle θ is perpendicular to the density gradient. Had we considered this geometry, Eq. (2.37) would have been replaced by $G = \frac{\pi \mathbf{k}_0 L(v_{\rm osc}/c)^2}{cos(\theta)}$. Pierre Michel derived a new formula for Raman gain that does not diverge at the turning point[2]. This formula is a path integral of a local gain rate along the Raman light ray that depends on the damping of the coupled Langmuir wave and the beat wave that results from the incident beam and scattered light interacting. The Rosenbluth gain formula can be retrieved from this gain formula when the Raman light rays are straight lines. Refraction (bending) of the rays remove the divergence. Before implementing this approach we first review the ray tracing of the plasma waves.

References

[2] P. Michel, M. J. Rosenberg, W. Seka, A. A. Solodov, R. W. Short, T. Chapman, C. Goyon, N. Lemos, M. Hohenberger, J. D. Moody, S. P. Regan, and J. F. Myatt, "Theory and measurements of convective raman side scatter in inertial confinement fusion experiments," *Phys. Rev. E*, vol. 99, p. 033 203, 3 Mar. 2019. DOI: 10.1103/PhysRevE.99.033203. [Online]. Available: https://link.aps.org/doi/10.1103/PhysRevE.99.033203.

[6] W. L. Kruer, "The Physics of Laser Plasma Interactions," in, ser. Frontiers in Physics, D. Pines (Ed.) Vol. 73, Redwood City, CA: Addison-Wesley, 1988.

[8] R. W. Boyd, *Nonlinear Optics, Third Edition*, 3rd. USA: Academic Press, Inc., 2008, ISBN: 0123694701.

[9] D. E. Hinkel, M. D. Rosen, E. A. Williams, A. B. Langdon, C. H. Still, D. A. Callahan, J. D. Moody, P. A. Michel, R. P. J. Town, R. A. London, and S. H. Langer, "Stimulated raman scatter analyses of experiments conducted at the national ignition facility," *Phys. Plasmas*, vol. 18, p. 056 312, 2011.

Chapter 3

Ray Tracing

In what follows, the ray tracing equations for EM and electron plasma waves are given without derivation. The derivation uses the ideas of the WKB theory [10] that is often used to solve wave equations that have slowly varying inhomogeneity. For example, it is used in quantum mechanics to solve the Schrödinger for weakly varying potentials. Notice that this has nothing to do with plasmas, and is very general. For example, classical mechanics is the geometrical optics (ray tracing) limit of quantum mechanics. In rays tracing, our plasma waves will behave like particles. For a derivation, see Sec. 7.2 (p. 352) in "Modern Classical Physics" by Thorne and Blandford.

As we have seen in Section 2.2, waves of a given type have a dispersion function $D(\omega, \mathbf{k})$. The frequency ω and wavenumber $\mathbf{k}$ for a wave are not arbitrary, but are related by the dispersion function by $D(\omega, \mathbf{k}) = 0$. When solved explicitly for, say, $\omega = \omega(\mathbf{k})$ we call this the dispersion relation. The dispersion function which is given implicitly for EM waves of a particular polarization in an unmagnetized plasma is:

$$D(\omega, \mathbf{k}) = -c^2k^2 + \omega^2 - \omega_{\rm pe}^2, \tag{3.1}$$

where $\omega_{\rm pe}$ is the electron plasma frequency, and c is the speed of light. The dispersion function for Langmuir (electron plasma) waves is similar:

$$D(\omega, \mathbf{k}) = -3v_{\rm Te}^2k^2 + \omega^2 - \omega_{\rm pe}^2, \tag{3.2}$$

where v_{Te} is the electron thermal velocity.

In ray tracing, the dispersion function can be used to construct a ray Hamiltonian D'. It completely describes the propagation of rays in the same way that the Hamiltonian in classical mechanics completely describes the trajectories of particles [11]:

$$D' = \left(\frac{\partial D}{\partial \omega}\right)^{-1} D. \tag{3.3}$$

For EM and EPWs the ray Hamiltonian D' can be taken to be

$$D' = \frac{1}{2\omega} D. \tag{3.4}$$

The reasons for this scaling are so that our rays will be parameterized by a t which is the physical time. To see how this arises, see Sec. 3.2 of the book "Ray Tracing and Beyond" by E.R. Tracy, A.J. Brizard, A.S. Richardson, and A.N. Kaufman.

Using Eq. (3.4) as a Hamiltonian, the ray position $\mathbf{x}$ and its wavevector $\mathbf{k}$ evolve in time in the ray phase space $(\mathbf{x}, \mathbf{k})$ according to Hamilton's equation (just like a mechanical particle where the wavevector $\mathbf{k}$ takes the place of the momentum $\mathbf{p}$). Hamilton's equation for our plasma wave "particle" are then:

$$\begin{aligned} \frac{\mathrm{d}\mathbf{x}}{\mathrm{d}t} &= -\nabla_{\mathbf{k}} D', \\ \frac{\mathrm{d}\mathbf{k}}{\mathrm{d}t} &= \nabla_{\mathbf{x}} D'. \end{aligned}$$

Substituting for the EM wave Hamiltonian, we get the ray equations for EM waves:

$$\frac{\mathrm{d}\mathbf{x}}{\mathrm{d}t} = \frac{c^2 \mathbf{k}}{\omega}, \tag{3.5}$$

$$\frac{\mathrm{d}\mathbf{k}}{\mathrm{d}t} = -\frac{\omega}{2}\frac{n_{\mathrm{e}}}{n_{\mathrm{c}}} \nabla_{\mathbf{x}} \log n_{\mathrm{e}}, \tag{3.6}$$

where $n_{\rm c} = \frac{m_e \omega_0^2}{4\pi e^2}$ is the critical density for EM waves of frequency ω. In an inhomogeneous plasma that is stationary (or changes very slowly in time) the frequency ω is constant.

From Eq. (3.5) it is seen that the ray position moves in the direction of the local wavenumber (momentum) with the local EM group velocity ($v_g = c^2\mathbf{k}/\omega$). The local wavenumber $\mathbf{k}$ "feels a force" (think $\mathbf{k} \sim \mathbf{p}$) that pushes the ray in a direction opposite the gradient of the electron density and with a strength that is proportional to $n_{\rm e}/n_{\rm c}$. Since the critical density $n_{\rm c}$ is a cutoff for EM waves, it is often helpful to think of EM rays as being repelled (reflected) by their cutoff ($\mathbf{k} \to 0$). This turns out to be true for all sorts of waves in general. Notice that the system of equations [Eqs. (3.5) & (3.6)] are first order in time. This means that the ray position and its wavevector must be specified at some initial moment in time.

We can do the same thing to get the ray equations for Langmuir waves too:

$$\begin{aligned} \frac{{\rm d}\mathbf{x}}{{\rm d}t} &= \frac{3v_{\rm Te}^2\mathbf{k}}{\omega}, \\ \frac{{\rm d}\mathbf{k}}{{\rm d}t} &= -\frac{\omega}{2}\frac{n_{\rm e}}{n_{\rm c}}\nabla_{\mathbf{x}}\log n_{\rm e} - \frac{3}{2}\frac{k^2 v_{\rm Te}^2}{\omega}\nabla_{\mathbf{x}}\log T_{\rm e}, \end{aligned}$$

where $T_{\rm e}$ is the spatially varying electron temperature. As for EM waves, the ray position moves in the direction of the local wavenumber but this time with the local plasma wave group velocity which depends on the electron temperature. Electron plasma waves (EPW) also exhibit a cutoff and it can be useful to think of EPW rays as being repelled (reflected) by their cutoff ($\mathbf{k} \to 0$). The local wavenumber $\mathbf{k}$ again "feels a force" (think $\mathbf{k} \sim \mathbf{p}$) that pushes the ray in a direction opposite the gradient of the electron density and with a strength that is proportional to $n_{\rm e}/n_{\rm c}$. For plasma waves there is also a force coming from gradients in electron temperature.

3.1 The use of ray tracing in laser-plasma experiments

The usual reason for ray tracing in ICF is because the laser light is the source of energy that will be used for the application - compressing a fusion target. The rays can be used to compute how much laser energy is absorbed and where it is absorbed (as a function of time). Furthermore, the size of the plasma is usually very large compared with the wavelength of the laser light, so solving Maxwell's equations numerically on such a large volume with sufficient resolution would be prohibitively expensive or impossible.

All that is needed are the initial conditions for a ray (the initial point in the ray phase space) $[\mathbf{x}(0), \mathbf{k}(0)]$ and we can find the ray at any other time. However, it is not enough to have one ray. In order to compute the electric field (or laser intensity) everywhere in the target we would need an infinite family of rays. In practical terms, a large number of incident rays that are distributed over the laser spot. Given the rays, the electric field intensity can be determined as a function of space (by interpolation) from which the absorption can be computed.

To specify the ray initial conditions relevant to an experiment, we need to know what the laser spot looks like at the position of the target. Of course we need to know the functional form for $n_{\mathrm{e}}(\mathbf{x})$, $T_{\mathrm{e}}(\mathbf{x})$ and their spatial derivatives. We usually get these from a radiation-hydrodynamics code. Our use of the rays will be somewhat different: Instead of computing absorption with rays we will compute SRS gain. This still requires a knowledge of the laser intensity as this is an important factor in the determination of gain.

3.2 Computing laser intensity in the plasma from rays

Given that the ray trajectories have been computed, as shown above for example, some extra information is required to compute the amplitude or intensity of the light wave along the trajectory. This information has to do with the properties of neighbouring rays.

To do this using the formal method of Tracy *et al.* Ray tracing and beyond [12], the extra information comes from computing the ray "focusing tensor" $\theta_{,\mathrm{ij}}$ along each ray:

$$\theta_{i,j} \equiv \frac{\partial^2 \theta}{\partial x^i \partial x^j},$$

Where θ is the phase along the ray. This phase can always be computed because we know the wavevector everywhere along the trajectory parameterized by time t. Remember that $\mathbf{k} = \nabla\theta$, so $\theta_{,\mathrm{ij}}$ is like the derivatives of the wavenumber:

$$\theta_{,ij} \equiv \frac{\partial k_j}{\partial x^i}.$$

The trace of the focusing tensor is the divergence of $\mathbf{k}$:

$$\theta_{,ii} \equiv \frac{\partial k_i}{\partial x^i} = \nabla \cdot \mathbf{k}.$$

For a 2-D case, and specializing for EM waves the following equations can be derived [12]:

$$\frac{\mathrm{d}\theta_{,zz}}{\mathrm{d}t} = D_{,zz} - \frac{c^2}{\omega}\left[\theta_{,zz}^2 + \theta_{,rz}^2\right], \tag{3.7}$$

$$\frac{\mathrm{d}\theta_{,rr}}{\mathrm{d}t} = D_{,zz} - \frac{c^2}{\omega}\left[\theta_{,rr}^2 + \theta_{,zr}^2\right], \tag{3.8}$$

$$\frac{\mathrm{d}\theta_{,rz}}{\mathrm{d}t} = D_{,rz} - \frac{c^2}{\omega}\left[\theta_{,zz}\theta_{,zr} + \theta_{,rz}\theta_{,rr}\right]. \tag{3.9}$$

Once this system is solved for the focusing tensor components $\theta_{,22}$ and $\theta_{,\mathrm{rr}}$ along the ray, then we get the action $\mathcal{J}$ (and amplitude A, intensity $I = A^2$) from solving

$$\frac{\mathrm{d}\log\mathcal{J}}{\mathrm{d}t} = D^{,zz}\theta_{,zz} + D^{,rr}\theta_{,rr}. \tag{3.10}$$

We note that the action $\mathcal{J}$ is related to the intensity I by $\mathcal{J} = A^2 D_\omega$, where A is the wave amplitude, and $D_{_\omega} = \partial D/\partial\omega = 2\omega$.

The derivatives of the dispersion function that are required in Eqs. (3.7) - (3.9) are

$$\begin{aligned} D^{,zz} = D^{r,r} &= -\frac{c^2}{\omega}, \\ D_{,zz} &= -\frac{1}{2\omega}\frac{\partial^2\omega_{\mathrm{pe}}^2}{\partial z^2} \\ D_{,rr} &= -\frac{1}{2\omega}\frac{\partial^2\omega_{\mathrm{pe}}^2}{\partial r^2} \\ D_{,rz} &= D_{,rz} = -\frac{1}{2\omega}\frac{\partial^2\omega_{\mathrm{pe}}^2}{\partial r\partial z}. \end{aligned}$$

These equations describe the effects of (swelling in intensity as the group velocity decreases), as well as the changes in wave intensity as neighbouring rays converge (focus) or diverge. These changes occur because of conservation of wave action.

If the plasma is of uniform density, then:

$$\frac{\mathrm{d}\log\mathcal{J}}{\mathrm{d}t} = -\frac{c^2}{\omega}\nabla\cdot\mathbf{k}. \tag{3.11}$$

Finally, we note that a more *ad-hoc* approach is used in radiation hydrodynamics codes. Typically the intensity change along a ray is estimated using its neighbours (that are discretely sampled). The divergence of the rays can be estimated by how much the area they span changes along the path and the approximate solution to the above equation [Eq. (3.11)] estimated.

3.3 Ray tracing summary

The equations defined in this chapter are sufficient to compute the intensity and ray trajectories of laser beams that are incident on a known plasma profile (n_e, T_e) subject to known initial conditions. This profile is typically known only at discrete points in space and time because it is computed numerically (by radiation-hydrodynamics code). Likewise, the solution to the ray equations must be obtained numerically. In the next chapter we describe the implementation of a numerical scheme that is used in Chapter 5 to compute SRS gain and to interpret experimental data.

References

[10] J. Heading, "An introduction to phase-integral methods," 1962.

[11] C. P. H. Goldstein and J. Safko, *Classical Mechanics*, 3rd. Pearson, 2002.

[12] E. R. Tracy, A. J. Brizard, A. S. Richardson, and A. N. Kaufman, *Ray Tracing and Beyond*. Cambridge, United Kingdom: Cambridge University Press, 2014.

Chapter 4

MATLAB Implementation of the Ray Tracing and SRS Gain Equations

In this chapter, we describe the simulation code that was developed and its operation. The purpose of the code is to simulate laser fusion experiments in order to figure out the mechanisms causing the scattered light that is detected in the physical experiment. A visual representation of the flow of the code is given in Fig. 4.1.

As seen in Fig. 4.1, the first step to the simulation code is to import a file containing the plasma variables. The most important being the plasma density and temperature. A radiation-hydrodynamics code called DRACO[13] simulates the experiment and writes the data to a file - a "DRACO file". This DRACO file contains information that is only an estimate of the hydrodynamics of the physical experiment. Currently, it remains difficult to actually measure the hydrodynamic profiles. The main information that is used from this file is the two dimensional density and temperature. The data is two dimensional as a rotational symmetry is assumed. All the information in this file is separated into 20 time slices which are 0.25 ns apart from each other. Most of the simulation work done was performed for a single time slice (i.e., by assuming steady state). From this DRACO file we obtain a 2 dimensional grid that has spatial limits of -807.616 μm to 1371.285 μm for the z (horizontal) axis and -1255.646 μm and 1255.646 μm for the r (vertical) axis.

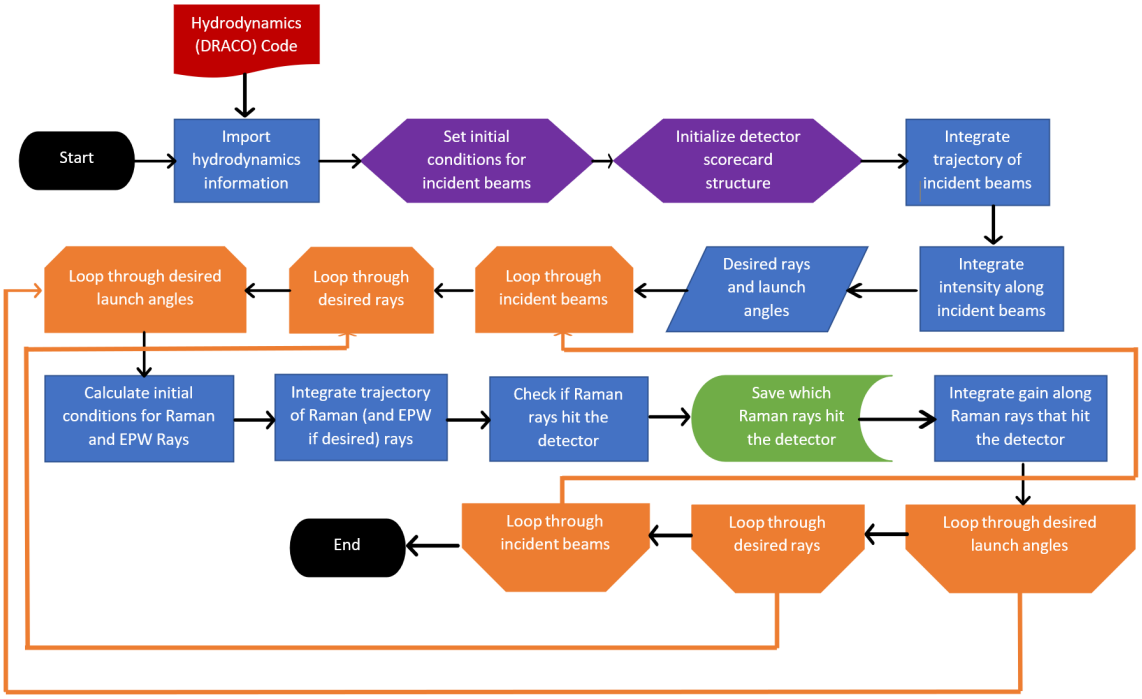

Figure 4.1: A visual representation of the simulation flow.

Next, the incident beams are created and their initial conditions set by the `makeRayBundle` function. This function takes a launch list (see Listing 4.1) as an argument and returns a ray bundle that can be integrated. The variable `rayBundle` is a cell array of ray structure and `launchList` is a structure that contains initial conditions and other necessary information. This function can also be used to create Raman at the detector location and work backwards to find where the detected Raman originates.

Listing 4.1: This code is used to create a structure that is passed to another function "`makeRayBundle`". This structure is a list of the desired properties of the ray bundle.

```
launchList.type = 'laserBeam';          % trigger for 'makeRayBundle'
launchList.mode = 'forward';            % Sets whether the rays advance in time 'forward'
                                        % or retrace its path 'backward'
launchList.nrays = 20;                  % Number of rays in the bundle
launchList.frequency = cnst.omega0; % Frequency of the light for this bundle in 1/sec


launchList.focalPt = [-400,0];          % Coordinates of center of spherical target
                                        % in microns
launchList.spot = struct('type','SG8','diameter',700);  % sets the beam diameter
angle = 180+(+23.3);                    % (degres) is measured from "target norm"
launchList.centroid = [cosd(angle),sind(angle)]; % unit vector in direction
                                                 % of beam propagation
launchList.translate = 5.0e3;           % distance in um from focus to
                                        % translate so that we are sure to
```

```
                                        % be far enough away to start
% Create a ray bundle
rayBundleB2 = makeRayBundle(launchList,rayGd);
```

Listing 4.2: The `makeRayBundle` function.

```
function rayBundle = makeRayBundle(launchList,rayGd,segLength,itmax)
bundleType = launchList.type;

switch bundleType
  case 'laserBeam'
    nrays = launchList.nrays;
    omega = launchList.frequency*ones(1,nrays);      % rad/sec
    centroid = launchList.centroid;    % direction vector [kz,kr]
                                       % norm to 1
    focalPt = launchList.focalPt;
    spotShape = launchList.spot;       % just a diameter for now
                                        % (e.g. 500 um)
    % initial ray positions (col vecs) in beam wavefront coords
    rayWavPositions = zeros(2,nrays);  % each column is a ray
    rayWavPositions(2,:) = linspace(-spotShape.diameter/2, ...
                                    spotShape.diameter/2,nrays); % microns

    rayNorm = [-1,0];

    angleB = atan2(centroid(2),centroid(1));
    angleA = atan2(0,-1);
    angle = angleB-angleA;

    % rotate to be parallel to direction and translate to 5 mm away
    rotMat = [cos(angle),-sin(angle);sin(angle),cos(angle)];
    rotPos = rotMat*rayWavPositions;

    % translate origin to focus
    transPos = rotPos+repmat(focalPt',1,nrays);

    % translate 5 mm away (outside of the plasma)
    translate = -(launchList.translate)*centroid';    % microns
    rayPositions = transPos+repmat(translate,1,nrays);
    % transport into plasma can be done here?

    % set the frequency depending on the mode
    switch launchList.mode
      case 'forward'
        rayBundle.frequency = omega;  % run time forwards
      case 'backward'
        rayBundle.frequency = -omega; % run time backwards
      otherwise
        error('bad mode in launchList')
    end

    lambdaum = 1.e6*(cnst.twopi*cnst.c./omega);     % um
    rayBundle.nc = 1.1e21./lambdaum.^2;
    rayBundle.name = 'laserBeam';
    rayBundle.type = 'EM';
    rayBundle.mode = 'forward';

  case 'RamanAtDetector'
       % Similar to the 'laserBeam' case
       ...
  otherwise
    error('not a valid beam type')
end

rayBundle.nrays = nrays;
rayBundle.direction = launchList.centroid;
rayBundle.rayICs = rayPositions;
```

```
rayBundle.trajs = cell(1,nrays);
rayBundle.halt = zeros(1,nrays); % to terminate a trajectory

% bring into the domain if required
if strcmp(launchList.type,'laserBeam') | strcmp(launchList.type,'RamanAtDetector')
    rayBundle = moveToDomain(rayBundle,rayGd,segLength,itmax);
end

end
```

To set the initial conditions for the incident light beams, there is a subfunction (used in the last if statement of `makeRayBundle`) called `moveToDomain`. This `moveToDomain` subfunction moves the initial position of the rays in the bundle to be within the simulation domain. These incident beams are then propagated towards the target using the function "`pushBundle`". This `pushBundle` function is used anytime any ray is propagated in the simulation. It solves the ray equations [Eqs. (3.1) and (3.2)] to advance the ray trajectory over a given interval of time.

Listing 4.3: This function (`pushBundle`) uses `ode45` to integrate the propagation of the rays in the simulation. This is the longest and most computing expensive portion of the code since it loops through all the rays in the ray bundle that are passed to the function and integrates the trajectory of each ray.

```
function bundleOut = pushBundle(rayBundle,rayGd,tStep,margin,npts)

if ~exist('margin','var')
    margin = [150 150 150 150];   % margin around domain in microns
end

if ~exist('npts','var')
    npts = 2000;                  % points to use in str line check
end

% Integrate all the rays in the bundle one at a time

for rayIdx = 1:rayBundle.nrays;

    % check to see if we need to move this ray
    if rayBundle.halt(rayIdx)
        continue  % skip to next ray (iteration of loop)
    end

    trajIsNew = isempty(rayBundle.trajs{rayIdx});
    waveType = rayBundle.type;

    if trajIsNew    % need IC's for trajectory
        if waveType == 'EM'
            x0 = rayBundle.rayICs(:,rayIdx)';  % position x0 is row vector here
            k0 = toDispSurface(x0,rayBundle,rayIdx,rayGd);
            tPrev = 0;                         % start from t=0
        else
            error('Currently new trajectories are for EM waves only')
        end
    else
        lastInfo = rayBundle.trajs{rayIdx}(end,:); % use the last time info
        x0 = lastInfo(2:3);                        % position row vector
```

```
        k0 = lastInfo(4:5);                    % wave vector row vector
        tPrev = lastInfo(1);
    end

    omega_ps = 1.e-12*rayBundle.frequency(rayIdx);
    dirn = sign(omega_ps);              % see which direction we're going
    tStop = tPrev+tStep;
    tSpan = [tPrev, tStop];
    ray0 = [x0, k0]';                   % initial condition (column vector)
                                        % in phase space for ode integrator

    % Integrate over the given time span
    if tStop > tPrev
        switch waveType
          case 'EM'
            [tr,yr] = ode45(@(t,y) odeEmRayFun(t,y,omega_ps, ...
                                               rayGd),tSpan,ray0);
          case 'EPW'
            [tr,yr] = ode45(@(t,y) odeLwRayFun(t,y,omega_ps, ...
                                               rayGd),tSpan,ray0);
          otherwise
            exit('invalid waveType')
        end

        newTraj = [tr,yr];    % Otherwise ode45 will return a struct

        withinMargin = inDomain(yr(end,1:2),rayGd,margin);
        if any(~withinMargin)
            rayBundle.halt(rayIdx) = 1;    % set halt flag for
                                           % out-of-margin
        end
        % attach solution to rayBundle structure
        if trajIsNew
            rayBundle.trajs{rayIdx} = newTraj;
        else
            % append to existing
            oldTraj = rayBundle.trajs{rayIdx}(1:end-1,:); % drop IC
            rayBundle.trajs{rayIdx} = [oldTraj; newTraj];
        end
      end  % the if tSpan..
end   % for loop over rays

bundleOut = rayBundle;

end
```

The `inDomain` subfunction used in `pushBundle` is very similar to `moveToDomain`. The `inDomain` subfunction is a check function that returns a Boolean true or false depending on whether or not the ray positions that are passed are within given margins of the domain of the simulation space. The `toDispSurface` subfunction is used to calculate the wavevector at either the initial ray position or the last position of the ray's trajectory. The other two subfunctions, `odeEmRayFun` and `odeLwRayFun`, are used to calculate the the right hand side of the ODE that is solved using the MATLAB function `ode45`.

Listing 4.4: The function `odeEMRayFun` interpolates the density and spatial variations in density along the ray trajectories. These interpolated values are then used to calculate the time derivatives of the rays' position and wavevector.

```
function dydt = odeEmRayFun(t,y,omega_ps,rayGd)

    global cnst

    clum  = (cnst.c)*(1.e-6); % speed of light in microns/ps
    ln10  = cnst.ln10;
    twopi = cnst.twopi;

    lambdaum = twopi*clum/abs(omega_ps); % vac wavelength microns
    kVac = abs(omega_ps)/clum;           % vacuum wavenumber 1/um
    nc = 1.1e21/lambdaum^2;              % crit density in 1/cm^3

    x = y(1:2);       % current position at phase space point y
    kVec = y(3:4);    % current ray wavevector at phase space point y

    goodPt = inDomain(x',rayGd);

    if goodPt
        % interpolation for current position
        [ti,bc] = pointLocation(rayGd.DT,x');  % Delauney triangles

        triValNe = rayGd.valsNe(rayGd.DT(ti,:));
        logNe = dot(bc',triValNe')';      % log10 of electron density
                                          %    disp(logNe)  % debugging
        netonc = 10^(logNe)/nc;

        triValDLogNedz = rayGd.valsDLogNedz(rayGd.DT(ti,:));
        dLogNedz = dot(bc',triValDLogNedz')';   % at phase space point
                                                %    disp(dLogNedz)

        triValDLogNedr = rayGd.valsDLogNedr(rayGd.DT(ti,:));
        dLogNedr = dot(bc',triValDLogNedr')';   % at phase space point
                                                %    disp(dLogNedr)

        dzdt = sign(omega_ps)*clum*kVec(1)/kVac;
        drdt = sign(omega_ps)*clum*kVec(2)/kVac;
        dkzdt = -0.5*ln10*omega_ps*netonc*dLogNedz;
        dkrdt = -0.5*ln10*omega_ps*netonc*dLogNedr;

        dydt = [dzdt,drdt,dkzdt,dkrdt]'; % column vector
    else
        % move ray in a straight line
        dzdt = sign(omega_ps)*clum*kVec(1)/kVac;
        drdt = sign(omega_ps)*clum*kVec(2)/kVac;
        dkzdt = 0.0;
        dkrdt = 0.0;

        dydt = [dzdt,drdt,dkzdt,dkrdt]'; % column vector
    end

end
```

After the incident ray bundles, representing the incident laser beams, are created and propagated far enough towards the target, these ray bundle structures can be saved and then loaded in a different simulation run in order to save some computation time. Next, the intensity of the incident rays are integrated along their trajectory

after an initial intensity is assigned to the rays based on the experimental parameters. For this work, the initial intensity of all the rays in both incident bundles are set to be the same. However, for future simulation runs the initial intensity could be different for every ray and each time slice in order to account for different beam profiles and laser pulse shapes.

Listing 4.5: The `mapIntensity` function interpolates the temporal damping rate along the trajectory of the passed light ray bundles and integrates the intensity.

```
function intensity = mapIntensity(rayBundle,rayGd)

    intensity = cell(1,rayBundle.nrays);

    for rayIndx = 1:rayBundle.nrays
        traj = rayBundle.trajs{rayIndx};

        ncForRay = rayBundle.nc(rayIndx);          % cm^-3

        gammaEM = interpOnTraj('gammaEM',traj,rayGd,ncForRay);
        time = traj(:,1);
        tSamp = time;          % the times where gammaEM is known (sampled)

        tspan = [time(1) time(end)];

        lnI0 = log(rayBundle.I0(rayIndx));

        sol = ode45(@(t,y) dlnIdt(t,y,tSamp,gammaEM),tspan,lnI0);

        logI = deval(sol,time)';

        intensity{1,rayIndx} = exp(logI);
    end
end

function outval = dlnIdt(t,lnI,tSamp,gammaEM)
%   returns the rhs to dlog(I)/dt = - gammaEM(t)

    gamma = -1.e-12*gammaEM;       % convert from s^-1 to ps^1 and
                                   % give the right sign

    if t < tSamp(1)
        outval = gamma(1);
    elseif t > tSamp(end)
        outval = gamma(end);
    else
        outval = interp1(tSamp,gamma,t);
    end

   % catch NaNs if any are encountered
   if isnan(outval)
       outval = 0;
   end

end
```

Once the incident ray bundles have been created, propagated, and have a known intensity along their trajectory, we can begin to simulate stimulated Raman scattering: We first choose which of the rays of the incident bundles (beams) to iterate

over, as well as an array of SRS launch angles ranging from -179 to -20 and 20 to 180 degrees with respect to the local wavevector at a given position on the incident ray. Typically, each beam is described by 20 ray trajectories, although this number is user selectable and can be increased if more resolution is required. The launch angles are distributed evenly within the given range. During this process, we need a way to measure what Raman scattered light is detected and the gain of each ray of the detected Raman light. A detector structure is created to save the detected Raman data to (Listing 4.6). The fields of this structure include the angular position and acceptance of the detector, information on the origin of each Raman ray, the detected frequencies, and gain values at the last point of a ray.

Listing 4.6: Shows how the information for detected Raman is collected and saved in a detector structure variable.

```
detector = struct(...
 'name', "default", ...      %  e.g. "FABS 32B"
 'angPos', [23,0], ...       %  position of detector [theta,phi] in degrees
 'angAccept',3, ...          %  acceptance angle in degrees
 'sourceBeams', [], ...      %  Array of incident rayBundle structs
 'sourceParams', [], ...     %  Descriptor for each row of freqs
                               % detector.source[1,1] = time in ns of hydro slice
                               % detector.source[1,2] = index of sourceBeams array
                               % detector.source[1,3] = SRS angle in degrees
 'frequencies',[], ...       %  store frequencies here
 'histogram',[], ...         %  frequencies in a row vector
 'RosGain',[], ...           %  store Rosenbluth gains here
 'RosGainHist',[], ...       %  Rosenbluth gain corresponding to 'histogram'
 'gain',[], ...              %  Pierre's gain
 'gainHist',[], ...          %  Pierre's gain corresponding to 'histogram'
 'filter', []);
```

The following process is repeated for each of the incident beam bundles included in a simulation run: For each incident ray bundle, hydrodynamic time slice, and SRS launch angle, these values are saved to the detector structure as a new row in `sourceParams` and create a new row in the `frequencies`, `RosGain`, and `gain` fields. Next, we iterate through all the desired rays of the incident bundle to simulate the creation, propagation, and detection of Raman light. The creation of the Raman light (and EPW if desired) is done through the function `RamanWavevectors_sh`. This function interpolates the density, temperature, scale length, and density gradient unit vector along the trajectory of the passed incident ray. These interpolated values are

used to calculate the wavevectors for Raman light rays and EPW rays for the desired SRS launch angle. There are three checks to make sure that the Raman that was created is physical. These checks are that the Raman wavevector is purely real, that the ray is below the Landau cutoff ($k^2\lambda_{\mathrm{De}}^2 \lesssim 0.9$), and that only inbound points on the incident beam create Raman.

Listing 4.7: The `getRamanWavevectors_sh` function.

```
function [srsBundle,epwBundle] = getRamanWavevectors_sh(traj,omega_ps, ...
                                                        rayGd, angle, ...
                                                        rayI15, range, inboundOnly, ...
                                                        itmax, landauC)

    global cnst
    cumps = (cnst.c)*1.e-6;        % in um/ps
    kvac = omega_ps/cumps;         % (omega_ps is a scalar) inverse microns
    lambdaVac = cnst.twopi/kvac;   % microns
    nc = 1.1e21/lambdaVac^2;       % cm^-3

    [nrows ncols] = size(traj);

    if isscalar(omega_ps)
        omega_ps = repmat(omega_ps,nrows,1);
    else
        error('omega_ps must be a scalar')
    end

    % default number of iterations
    if ~exist('itmax','var')
        itmax = 5;
    end

    % default Landau cutoff
    if ~exist('landauC','var')
        landauC = 0.3;    % maximum allowable k*lambdaDebye
    end

    % default inboundOnly is true (no SRS after nc/4 is reached)
    if ~exist('inboundOnly','var')
        inboundOnly = true;
    end

    % default range is max range
    if ~exist('range','var')
        range = [350 750];
    end

    % For each point on ray we want a density, temperature, and density
    % gradient information
    neList = interpOnTraj('valsNe',traj,rayGd);
    teList = interpOnTraj('valsTe',traj,rayGd);    % eV
    gradStuff = interpOnTraj('unitGrad',traj,rayGd); % [z r L^-1]

    if ncols == 4
        xLoc  = traj(:,1:2);    % (Z, R)     (nrowsx2)
        kvecs = traj(:,3:4);    % (kZ,kR)    (nrowsx2)
    elseif ncols == 5
        tt = traj(:,1);         % times
        xLoc  = traj(:,2:3);    % (Z, R)
        kvecs = traj(:,4:5);    % (kZ,kR)
    end
```

```
unitGrad = gradStuff(:,1:2);
inverseL = gradStuff(:,3);

% Compute vosc/c
voscToc = (cnst.voscToC).*sqrt(rayI15).*lambdaVac; % check shape
voscToc2 = voscToc.^2;

% normalized scale length: (omega_0 L/c)
%
inverseLFloor = 0.001; % Smallest allowable value of inverseL
inverseL(inverseL<inverseLFloor) = inverseLFloor;
L = 1./inverseL;                    % should check for zeros!
Lnorm = (omega_ps/cnst.cumps).*L;   % dimensionless

% incident light wavevector magnitude for each point
k0 = sqrt(kvecs(:,1).^2 + kvecs(:,2).^2);  % um^-1 (nrowsx1)

k0Hat = kvecs./[k0 k0];   % unit vector in the direction of k0

% plasma paramters on the ray points
ne = 10.^(neList);      % cm^-3
neTonc = ne/nc;
wpeTow0 = sqrt(neTonc);
lamDeb2 = (cnst.lamDebye)^2*teList./ne;     % cm^2
lamDebum2 = 1.e8*lamDeb2;                   % um^2

outBound = find(neTonc >= 0.25); % indices for outbound points

if isempty(outBound)
    lastInboundIdx = numel(neTonc);
else
    lastInboundIdx = outBound(1);
end

rotMat = [cosd(angle),-sind(angle);sind(angle),cosd(angle)];

% kSRSHat is rotated counterclockwise by "angle" degrees from k0Hat
for i = 1:nrows
    columnVec = rotMat*[k0Hat(i,1);k0Hat(i,2)];
    kSRSHat(i,1) = columnVec(1);
    kSRSHat(i,2) = columnVec(2);
end

kSRSMag = kvac.*sqrt(1-2.*sqrt(neTonc));
kSRS = kSRSMag.*kSRSHat;
kLangmuir = kvecs-kSRS;
k = sqrt(kLangmuir(:,1).^2 + kLangmuir(:,2).^2);
kHat = kLangmuir./k; % Langmuir unit wavevector
k2lam2 = (k.^2).*lamDebum2;

% dimensionless EPW wavevector used in Rosenbluth gain calculation
%
dimlessEPWFac = (cnst.cumps^2.*k.^2)./omega_ps.^2;

isRealK = imag(kSRSMag) == 0;               % logical vectors
isBelowLandau = abs(k2lam2) <= landauC^2;
isInbound = (1:numel(k))' <= lastInboundIdx;

freqEPW = omega_ps.*wpeTow0.*sqrt(1+3*k2lam2);         % ps^-1
%freqEPW = omega_ps.*wpeTow0.*(1+3/2*k2lam2);         % ps^-1
freqSRS2 = (omega_ps.*wpeTow0).^2 + cumps^2*kSRSMag.^2;  % ps^-2
freqSRS = sqrt(freqSRS2);                                % ps^-1
vacWavlSRS = cnst.twopi*cumps./freqSRS;  % microns
ncSRS = 1.1e21./vacWavlSRS.^2; % cm^-3
neToncSRS = ne./ncSRS;
inRange = (vacWavlSRS >= range(1)/1000) & (vacWavlSRS <= range(2)/1000);

if inboundOnly
```

```
    goodidxs = find(isRealK & isBelowLandau & isInbound & inRange);
else
    goodidxs = find(isRealK & isBelowLandau & inRange);
end


% Get the times
%
if exist('tt','var')
    ttgood = tt(goodidxs);
else
    ttgood = zeros(1,numel(goodidxs));
end
% density dependent part of Rosenbluth gain (alpha)
%
alphaFac1 = 1./(1-sqrt(neTonc)); % incident wave

alphaFac2  = 1./sqrt(1-neToncSRS); % SRS wave
alphaFac = alphaFac1.*alphaFac2;

% angular dependent part of Rosenbluth gain (beta)
%
cosPhi = abs(dot(unitGrad,kSRSHat,2));
cosTheta = abs(dot(unitGrad,kHat,2));

% checks for small values (smaller than a set floor value) of cosPhi
% and cosTheta
cosFloor = 0.01; % Smallest allowable value of cosines
cosPhi(cosPhi<cosFloor) = cosFloor;
cosTheta(cosTheta<cosFloor) = cosFloor;

betaFac = cosPhi.*(cosTheta.^2);

otherFacs = alphaFac./betaFac;

% Calculate Rosenbluth gain
% Calculated as a column vector
RosGain = (cnst.pi/4).*Lnorm(goodidxs).*(voscToc2(goodidxs)) ...
    .*dimlessEPWFac(goodidxs).*otherFacs(goodidxs);

xs = xLoc(goodidxs,:);          % row vector (z r)
ks = kLangmuir(goodidxs,:);     % row vector (kz kr)

epwBundle.name = 'plasmaWave';
epwBundle.type = 'EPW';
epwBundle.mode = 'forward';
epwBundle.nrays = numel(goodidxs);
epwBundle.halt = zeros(1,numel(goodidxs));
epwBundle.frequency = 1.e12*freqEPW(goodidxs)';   % (row vec) s^-1
epwBundle.trajs = cell(1,numel(goodidxs));

% put in an intial condition for each trajectory
for idx = 1:numel(goodidxs)
    % needs to be a row vector: t, z, r, kz, kr
    epwBundle.trajs{idx} = [ttgood(idx) xs(idx,:) ks(idx,:)];
end

xs = xLoc(goodidxs,:);          % row vector (z r)
ks = kSRS(goodidxs,:);     % row vector (kz kr)

srsBundle.name = 'srsLight';
srsBundle.type = 'EM';
srsBundle.mode = 'forward';
srsBundle.nrays = numel(goodidxs);
srsBundle.halt = zeros(1,numel(goodidxs));
srsBundle.frequency = 1.e12*freqSRS(goodidxs)'; % row vec 1/sec
lam0 = (cnst.twopi)*(cnst.cumps)./freqSRS(goodidxs)';
srsBundle.nc = 1.1e21./lam0.^2; % cm^-3 for use in pushBundle()
```

```
    srsBundle.trajs = cell(1,numel(goodidxs));
    srsBundle.RosGain = RosGain'; % Converted to a row vector
    srsBundle.k0res = kvecs(goodidxs,:)';
    srsBundle.a0 = 0.85e-9.*sqrt(rayI15(goodidxs).*10^15.*lambdaVac.^2)';

    % put in an intial condition for each trajectory
    for idx = 1:numel(goodidxs)
        % needs to be a row vector: t, z, r, kz, kr
        srsBundle.trajs{idx} = [ttgood(idx) xs(idx,:) ks(idx,:)];
    end

end
```

After the Raman rays and EPW rays are created, we use `pushBundle` to propagate the rays. For the Raman light rays, there is a function that checks if the Raman has been propagated to where the change in direction of the trajectory of the rays is within a specified limit (i.e., it has exited the plasma). This function takes an argument that sets this limit to change in direction in degrees per picoseconds, as well as can check if the rays have reached a certain density. Once the Raman rays have reached the point that satisfied the given conditions we check to see which rays hit the detector. Rays that hit have their frequencies and gains saved to the detector structure. The gains are computed by performing an integral along the ray path of the scattered Raman light. The formula is given in Chapter 5. The way we check to see if a Raman ray hits the detector is through a function called `checkDetector` that iterates through all the rays in the passed Raman bundle and checks the angular direction of the wavevector in the last point along the trajectory falls within the acceptable range. The acceptable range depends on the actual physical properties of the detector. For this work the angle is 23 ± 3 degrees.

Listing 4.8: This evaluates the integrated gain of the Raman rays. This function uses the gain formula from Pierre Michel's paper[2].

```
function gain = gainMap(rayBundle,rayGd,rays)

global cnst

if ~exist('rays','var')
    rays = 1:rayBundle.nrays;
end

gain = zeros(1,length(rays));

for srsRay = rays
    trajLength = size(rayBundle.trajs{1,srsRay},1);

    % all wavevectors in inverse microns
```

```
    kSVec = rayBundle.trajs{1,srsRay}(:,4:5);
    kS = sqrt(kSVec(:,1).^2 + kSVec(:,2).^2);
    k0res = repmat(rayBundle.k0res(:,srsRay)',trajLength,1);
    kBVec = k0res - kSVec;
    kB = sqrt(kBVec(:,1).^2 + kBVec(:,2).^2);

    % all frequencies in rad/sec
    %omegaB = cnst.omega0 - srsBundle2.frequency(1,srsRay);
    ne = interpOnTraj('valsNe',rayBundle.trajs{1,srsRay},rayGd);
    ne = 10.^ne;
    omegaP = (cnst.wpe).*sqrt(ne);
    omegaPRes = omegaP(1);

    nc = rayBundle.nc(srsRay); %cm^-3
    gamma = interpOnTraj('gammaEM',rayBundle.trajs{1,srsRay},rayGd,nc);
    nu_ei = gamma.*nc./ne; %s^-1
    Te = interpOnTraj('valsTe',rayBundle.trajs{1,srsRay},rayGd,nc); %eV
    vThermal = 4.19e11.*sqrt(Te); %um/s

    omegaB = sqrt(omegaPRes.^2 + 3.*(kB.^2.*vThermal.^2));

    a0 = rayBundle.a0(srsRay);
    D = omegaB.^2 - omegaP.^2 - 3.*(kB.*vThermal).^2;

    lamD = 7.43e6.*sqrt(Te./ne); %um
    kLam = kB.*lamD;
    nuLan = omegaP.*sqrt(cnst.pi/8).*((1+3.*kLam.^2)./(kLam.^3)).*...
        exp(-(1./(2.*kLam.^2)+3/2));

    nu = nuLan + (omegaB.^2./omegaP.^2).*nu_ei;
    integrand = ((kB.^2.*a0.^2.*omegaP.^2)./(4.*kS))...
        .*((2.*nu.*omegaB)./(D.^2 + 4.*nu.^2.*omegaB.^2)); %inverse microns

    pathLength = computePathLength(rayBundle,srsRay);

    allGain = cumtrapz(pathLength{1,srsRay},integrand);
    gain(1,srsRay) = allGain(end);

end
end
```

Once the fields of the detector structure have been completely filled out, synthetic diagnostics can be generated. In addition, several plotting functions were written, but are not described here. Examples of synthetic diagnostics and various plots can be found in Chapter 5.

References

[2] P. Michel, M. J. Rosenberg, W. Seka, A. A. Solodov, R. W. Short, T. Chapman, C. Goyon, N. Lemos, M. Hohenberger, J. D. Moody, S. P. Regan, and J. F. Myatt, "Theory and measurements of convective raman side scatter in inertial confinement fusion experiments," *Phys. Rev. E*, vol. 99, p. 033 203, 3 Mar. 2019. DOI: 10.1103/PhysRevE.99.033203. [Online]. Available: https://link.aps.org/doi/10.1103/PhysRevE.99.033203.

[13] P. B. Radha, V. N. Goncharov, T. J. B. Collins, J. A. Delettrez, Y. Elbaz, V. Y. Glebov, R. L. Keck, D. E. Keller, J. P. Knauer, and J. A. Marozas, "Multidimensional analysis of direct-drive, plastic-shell implosions on OMEGA," *Phys. Plasmas*, vol. 12, 056307, 2005. DOI: http://dx.doi.org/10.1063/1.1882333. [Online]. Available: http://scitation.aip.org/content/aip/journal/pop/12/5/10.1063/1.1882333.

Chapter 5

Identification of stimulated Raman side scattering in near-spherical coronal plasmas

5.1 Introduction

This chapter describes the application of the previously described MATLAB code, developed as part of the thesis work, to investigate SRS that has been observed in recent experiments. The experiments were performed on the four beam OMEGA EP laser at the Laboratory for Laser Energetics at the University of Rochester. The analysis is based on hydrodynamic simulations that were performed by Dr. Andrey Solodov (of the University of Rochester) using the DRACO radiation-hydrodynamics code.

As we describe in Section 5.2, a scattered light diagnostic was implemented in these experiments. It was able to collect scattered light, in the SRS range of frequencies, that falls within a sub-aperture of one of the four OMEGA EP beams. Somewhat surprisingly, a large SRS signal was observed, spanning a wide frequency range. The observation of large levels of SRS was previously thought to occur in very large, hot, plasmas only (for typical direct-drive laser intensities) i.e., requiring MJ-class laser facilities, such as the NIF [14]. Indeed, no SRS signatures are observed at all in direct-drive ICF experiments performed on LLE's 60 beam OMEGA laser.

The results of these calculations (Sec. 5.4), provide an explanation of the observations in the form of stimulated Raman sidescattering. We believe the results, that have been obtained, represent a significant advance in terms of our understanding of laser-plasma interactions relevant to direct-drive ICF and directly-driven target experiments in general.

5.2 Experimental configuration

We focus on one type of experiment out of the several that have been recently described in Rosenberg *et al* [7]. These are spherical targets with one side illumination and have characteristics that we consider generic for all direct drive schemes: Namely, that the isodensity contours in the underdense corona are near-spherical and that multiple beams overlap (four in this case).

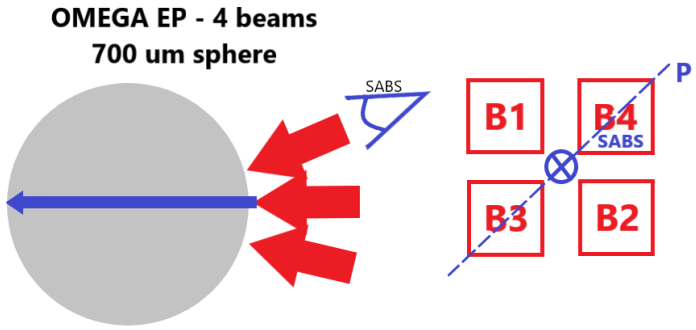

Figure 5.1: A schematic representation of spherical target experiments on OMEGA EP. The target is illuminated from one side by 1–4 beams (numbered B1–B4) in the inset. The dashed line denotes the plane containing the beam symmetry axis (solid arrow) and the centroids of beams B3 and B4.

A schematic diagram is shown in Fig. 5.1. In these experiments, between 1 and 4 beams were used to illuminate spherical polystyrene (CH) targets of 700 μm diameter. The incident beams had a super-Gaussian radial intensity profile with a nominal beam diameter of 750 μm. Each beam is polarized in the vertical direction. The laser pulse shapes were either 2 ns square or 4 ns linear ramp. The peak vacuum focused intensity of each beam was $I = 2 \times 10^{14}\,\mathrm{W/cm^2}$. A sub-aperture backscatter station (SABS),

located in the aperture of beam B4, collected backscattered light and passed it to streaked spectrometer. An example of a typical scattered light spectrum is shown in Figure 5.2. The streaked spectrometer recorded scattered light in the wavelength range of (400–750) nm, however in most cases a long pass filter was applied which blocked signal for wavelengths shorter than 630 nm.

The 630 nm long pass filter (e.g., as seen in Figs. 5.3a and 5.3b) was applied in most of the experiments performed by Rosenberg *et al.* because their focus was on the spectroscopy of near 700 nm scattered light and the strong signal at shorter wavelengths was a nuisance. Unfortunately, it does complicate the comparison of our predictions with experiment. We hope our findings will motivate further experiments of this kind.

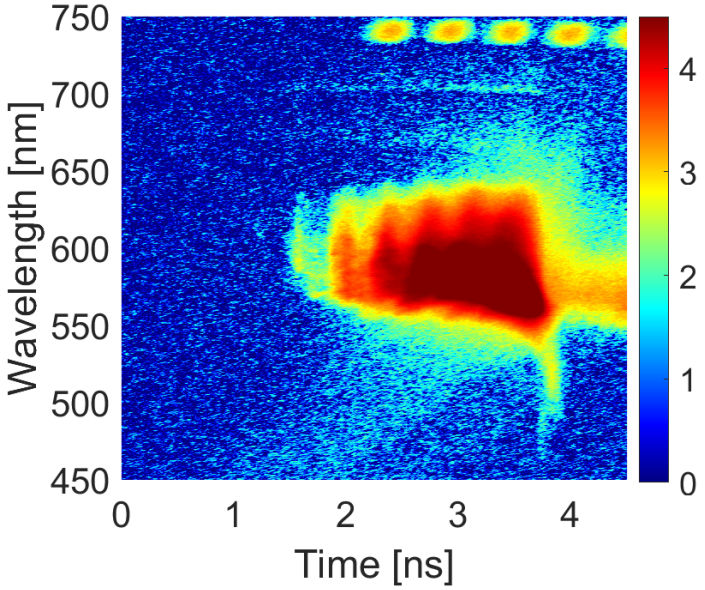

Figure 5.2: Temporally streaked scattered light spectrum for shot # 30575 in which a 700 μm spherical target was irradiated with a 4-ns ramped pulse peaking at $I = 2 \times 10^{14}$W/cm^2. The spectrum indicates a significant SRS reflectivity in the underdense corona.

The ∼700 nm spectroscopy was motivated by the fact that, in OMEGA-scale coronal plasmas, two-plasmon decay (TPD), which is the decay of an electromagnetic wave (EMW) into two Langmuir waves (LWs), is the dominant instability. However, planar experiments at NIF [14] showed strong absolute SRS signatures at ∼700 nm,

rather than the characteristic TPD doublet. As NIF experiments have a much longer density scale length, $L_{\rm n} \sim 600$ μm and higher electron temperature, $T_{\rm e} \sim 4-5$ keV, than OMEGA-scale ones ($L_n \sim 150$ μm, $T_e \sim 2$ keV), the OMEGA EP experiments were conducted to understand $n_c/4$ interaction regimes for hydrodynamic conditions intermediate between the two [7]. The goals of this work are distinct and two fold: One is to investigate the origins of the spectral features observed in the scattered light spectrum over the whole Raman scattering range of frequencies. The other is to investigate the state-of-the art for modeling such scattering.

5.3 Ray-based model predictions of the SRS scattered light spectrum

Our ray tracing analysis, motivated by the desire to understand the spectral features of the scattered observed in the experiments over the Raman range of frequencies, is based on the path integral method for computing sidescatter gain as described in Michel *et al* [2]. Figure 5.3 gives another example of scattered light data using a different combination of beams.

As simulating SRS over the whole interaction region (Fig. 5.4) is a computationally expensive proposition (although potentially possible, particularly with temporal wave-envelope codes) we choose a geometrical optics (or ray tracing) approach. The geometrical optics approximation is valid for the incident beams, absent nonlinear interactions even in the presence of weak absorption or growth. We assume the same is true for SRS reflected light and the associated EPW such that the amplitude A of all waves have an eikonal form: $A = \tilde{A} \exp\left[i\theta(\mathbf{x}) - i\omega t\right]$ (we assume the plasma is time independent, as justified below, so that the phase is time independent). The eikonal equation for each wave type is solved using ray tracing.

The dispersion function $D(\omega, \mathbf{k})$ for a particular wave type can be used to construct a ray Hamiltonian $D' = \left(\partial D/\partial\omega\right)^{-1} D$ that describes the propagation of rays. Using this Hamiltonian, the ray position $\mathbf{x}(t)$ and its wavevector $\mathbf{k}(t) \equiv \nabla_{\mathbf{x}}\theta(\mathbf{x})$ evolve in

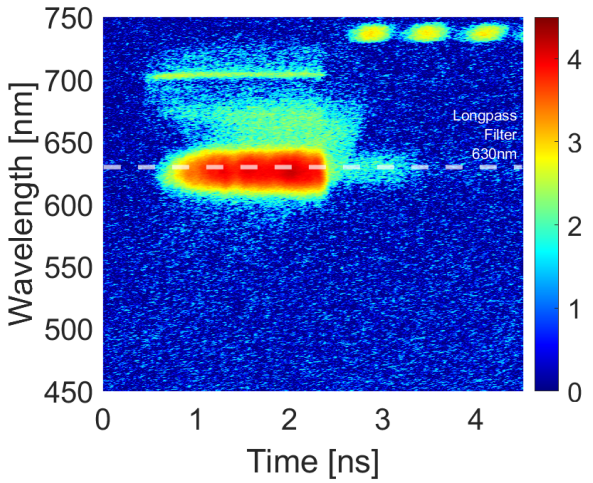

(a)

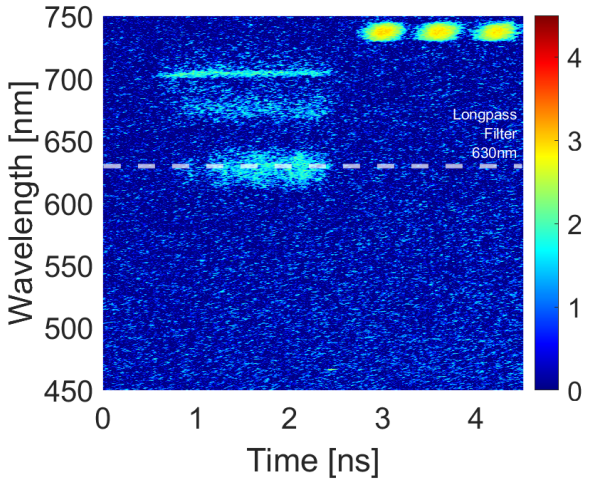

(b)

Figure 5.3: Streaked scattered light spectrum for experiments with a 2-ns laser pulse shape using beams B3 and B4 only (shot # 32063) (a) and B1 and B2 only (shot # 32064) (b). The laser intensity was the same in both cases ($I = 2 \times 10^{14}\,\mathrm{W/cm^2}$). The signal originating from beams B1 and B2 is over two orders of magnitude smaller than that from beams B3 and B4 (Fig. 5.1).

time in the ray phase space $(\mathbf{x}, \mathbf{k})$ according to Hamilton's equations:

$$\frac{\mathrm{d}\mathbf{x}}{\mathrm{d}t} = -\nabla_{\mathbf{k}} D', \tag{5.1}$$

$$\frac{\mathrm{d}\mathbf{k}}{\mathrm{d}t} = \nabla_{\mathbf{x}} D'. \tag{5.2}$$

Substituting for the EM wave dispersion function $D = D_{\mathrm{EM}} \equiv \omega^2 - c^2k^2 - \omega_{\mathrm{pe}}^2(\mathbf{x})$, we get the ray equations for EM waves:

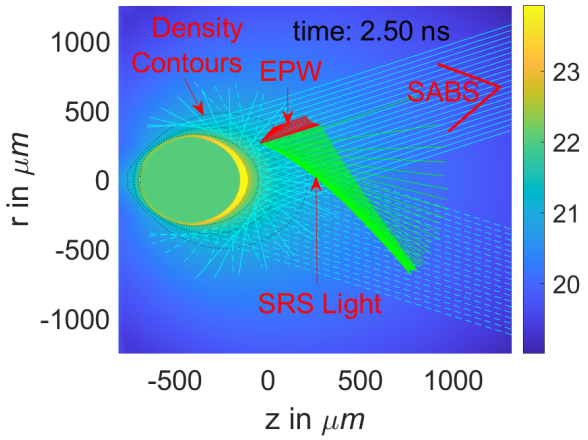

(a)

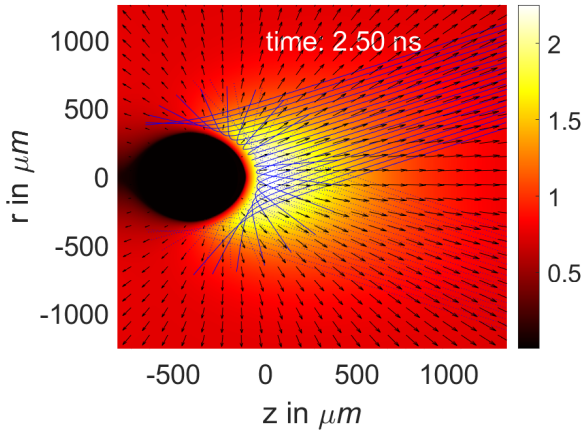

(b)

Figure 5.4: Predicted hydrodynamic conditions for shot # 30577. Density profile, ray trajectories [incident in cyan, EPW in red, and SRS in green] (a), temperature profile, and flow velocity [black arrows; length gives magnitude in arbitrary units] (b) used in the 2-D ray tracing simulations. Black dashed lines (a) show constant density contours (from inner most to outer most, n_c, $n_c/4$, and $n_c/10$)

$$\frac{d\mathbf{x}}{dt} = \frac{c^2\mathbf{k}}{\omega} = \mathbf{v}_{g,t}, \tag{5.3}$$

$$\frac{d\mathbf{k}}{dt} = -\frac{\omega}{2}\frac{n_e}{n_c}\nabla_{\mathbf{x}} \log n_e, \tag{5.4}$$

where c is the speed of light in vacuum, n_e is the electron density, and n_c $[= m_e\omega^2/(4\pi e^2)]$ is the critical density for EM waves of frequency ω with e and m_e being the electron charge and mass, respectively. Repeating this process for Langmuir waves $[D = D_{EPW} \equiv \omega^2 - 3v_{Te}^2k^2 - \omega_{pe}^2(\mathbf{x})]$ results in:

$$\frac{\mathrm{d}\mathbf{x}}{\mathrm{d}t} = \frac{3v_{\mathrm{Te}}^2\mathbf{k}}{\omega} = \mathbf{v}_{\mathrm{g,l}}, \tag{5.5}$$

$$\frac{\mathrm{d}\mathbf{k}}{\mathrm{d}t} = -\frac{\omega}{2}\frac{n_{\mathrm{e}}}{n_{\mathrm{c}}}\nabla_{\mathbf{x}}\log n_{\mathrm{e}} - \frac{3}{2}\frac{k^2 v_{\mathrm{Te}}^2}{\omega}\nabla_{\mathbf{x}}\log T_{\mathrm{e}}, \tag{5.6}$$

where $T_{\mathrm{e}}(\mathbf{x})$ is the spatially varying electron temperature and $v_{\mathrm{Te}} = (T_e/m_e)^{1/2}$ is the electron thermal velocity. Temperature variations cause refraction of the EPW, but it is a much weaker effect that variations in electron density $[O(k^2\lambda_{\mathrm{De}}^2)]$. Landau damping typically restricts $k\lambda_{\mathrm{De}} \lesssim 0.3$, so $k^2\lambda_{\mathrm{De}}^2 \lesssim 0.9$, where $\lambda_{\mathrm{De}} = (T_e/4\pi n_e e^2)(1/2)$ is the electron Debye length.

Equations (5.3)–(5.6) assume the plasma profile is stationary (unchanging in time) and therefore the frequency for each corresponding wave is constant along the ray [equal to its initial frequency (Sec. 5.3.1)]. This is a good approximation for our purposes as we concentrate on times that are late enough to avoid the initial phase of corona formation [$t \lesssim (1-2)$ ns]. We also assume that the hydrodynamic profile is fixed for the time of propagation of the ray, t_{prop}. This is a good approximation since $t_{\mathrm{prop}} \ll t_{\mathrm{hydro}}$, where t_{hydro} is the characteristic time associated with variation of the hydrodynamic quantities.

In the absence of measured hydrodynamic profiles, we use simulated profiles for the hydrodynamic quantities (e.g., n_{e} and T_{e}). These have been obtained using the DRACO radiation-hydrodynamics code[13]. Examples of such plasma profiles are shown in Fig. 5.4 which shows the electron plasma density (Fig. 5.4a) and the electron temperature (Fig. 5.4b) at a time $t = 2.5$ ns from the start of the laser pulse. The simulated experiment had a 4 ns linear ramp laser pulse with a peak (overlapped) laser intensity of $I = 8.5 \times 10^{14}\,\mathrm{W/cm^2}$. The hydrodynamic simulations are 2D and assume rotational symmetry of the hydrodynamic variables about the z axis. Notice that the electron temperature is quite inhomogeneous, having a peak temperature of $\sim 2.2\,\mathrm{keV}$ in the area of beam overlap and falling to about half this value at the beam wings. This is interesting as Raman is thought to be usually favored in the

high temperature regime. The (radial) density scale length is in the range of 200 – 300 μm in the $n_c/4$ region.

The ray equations [Eqs. (5.3)–(5.6)] are also solved in two spatial dimensions. However, unlike the hydrodynamics, these are solved in the 2-D plane that contains the symmetry axis of the four beams together with the centroids of beams B3 and B4. This plane is shown schematically in Fig. 5.1 by the dashed blue line labelled "P". This simplifying assumption is motivated by the observation that beams B1 and B2 (that lie out of this plane) contribute very little to the observed SRS signal in the SABS detector. Figure 5.3 shows the detected scattered light for an experiment in which only beams B3 and B4 were fired (Fig. 5.3a) and an experiment in which only beams B1 and B2 were used (Fig. 5.3b). As the plasma profile is not expected to differ greatly between these two cases, it can be seen that most of the light collected in SABS originates from beams B3 and B4. Note that the color scale is logarithmic, showing that the difference is approximately two orders of magnitude.

5.3.1 Ray initial conditions for the incident laser light

In addition to the plasma profiles, Eqs. (5.3)–(5.6) require initial conditions to be specified. As these are first order differential equations in time, we must specify the initial ($t = t_0$) position $\mathrm{x}(t_0)$ and wave vector $\mathbf{k}(t_0)$ for each ray. Describing each beam with N rays, the initial position $\mathbf{x}_i(t_0)$ of the i^{th} ray ($i = 1, N$) is chosen to be on the right simulation boundary, where it is intersected by a beam, while the directions $\mathbf{k}_i(t_0)/|\mathbf{k}_i(t_0)|$ are fixed at an angle of $+23^\circ$ for beam B4 and -23° for beam B3 (angle with respect to z axis, pointing from the center of the target). The magnitudes $|\mathbf{k}_i|$ are chosen so that the rays lie on the dispersion surface $D(\omega, \mathbf{k}_i(t_0); \mathbf{x}_i(t_0)) = 0$.

For the wavefield of each beam to be constructed in the SRS active region (Sec. 5.3.2 provides more details), the initial phase $\theta[\mathbf{x}_i(t_0)]$, focusing tensor $\partial_i\partial_j\theta[\mathbf{x}_i(t_0)]$ [12], and intensity $I[\mathbf{x}_i(t_0)]$ must be specified at $t = t_0$ for each ray. Of these, the most important is the intensity along the ray as this is directly required for computation

of the SRS gain. Given the initial intensity, the intensity can be easily computed at any point on the ray, using Eq. (5.11), so long as a caustic surface is not encountered[12]. For the purposes of computing SRS gain (Sec. 5.3.2), caustics are not encountered. The intensities are chosen to be consistent with the intensity profile of a beam smoothed by a phase plate as described in Sec. 5.3.2. Figures 5.4a and 5.4b show the ray trajectories that result. Ray integration is stopped when the time t is sufficiently large for the ray to have reflected from its turning point. The rays for beams B3 and B4 are overlaid on a plot of the electron density in Fig. 5.4a, while the beam B4 rays are overlaid on a plot of the electron temperature and plasma flow velocity in Fig. 5.4b. The plasma profiles in both cases are taken at time t = 2.5 ns from the start of the laser pulse. Since the hydrodynamics is fixed during ray integration, this time is merely a parameter.

5.3.2 Raman scattering instability with rays

A ray splitting procedure has been adopted which simulates SRS in the following way: After we launch the incident beams towards the target, we sample points along the incident ray trajectories and check to see if these points can support three wave resonance. This is the case if, at the point $\mathbf{x}$, solutions exist to the three wave resonance conditions

$$\omega_0 = \omega_s + \omega_{EPW} \tag{5.7}$$

$$\mathbf{k}_0 = \mathbf{k}_s + \mathbf{k}_{EPW}, \tag{5.8}$$

where ω_0 and $\mathbf{k}_0$ are the local frequency and wavenumber of the incident light at the particular point $\mathbf{x}$ on the incident ray, and the frequencies and wavenumbers of the scattered light and EPW satisfy their local dispersion relations: $D_{EM}(\omega_s, \mathbf{k}_s; \mathbf{x}) = 0$ and $D_{EPW}(\omega_{EPW}, \mathbf{k}_s; \mathbf{x}) = 0$. The direction of the scattered wave vector is chosen from the range of all positive angles, with the exception of near forward scatter ($< \pm 5^\circ$),

with respect to the $\mathbf{k}$ vector of the incident light. The choice of direction is repeated for several rays originating from the same point to sample all possible scattering directions, i.e., we do not assume side scatter.

If a sampled point can support three wave resonance and the EPW is not heavily damped (i.e., beyond the Landau cutoff) a Langmuir wave and a Raman scattered light wave are launched using $\mathbf{x}$ and $\mathbf{k}_{\mathrm{EPW}}$, $\mathbf{k}_{\mathrm{s}}$ as their initial conditions, respectively. The Raman light, of frequency ω_{s}, is propagated using the ray equations [Eqs. (5.3) and (5.4)], the Langmuir waves can also be propagated if desired [while we make no use of the EPW here, we feel that the trajectories are instructive; they will be used to compute Thomson scattering spectra in future studies]. Next, the trajectory of the Raman light is checked to see if it would hit the detector (SABS). This is accomplished by checking the direction of the Raman light to see if its angle of propagation falls within the angular acceptance of the detector on exiting the plasma. If the Raman ray hits the detector, a gain is computed by evaluating a path integral along its trajectory, using Eq. (5.9) as described below. Both the gain and scattered light frequency are saved to a detector scorecard to be used in the analysis leading to Figs. 5.5 and 5.9.

Equation (5.9), derived recently by Michel *et al.* [2], has been shown to accurately compute the spatial gain for SRS (including SRS side scatter) when the instability is convectively unstable. It assumes a local, driven, EPW response (not requiring the EPW rays):

$$G = \int_s \frac{k_b^2 |a_0|^2 \omega_{\mathrm{p}}^2}{4 k_{\mathrm{s}}} \frac{2\nu\omega_{\mathrm{b}}}{D_{\mathrm{EPW}}^2(\omega_{\mathrm{b}}, \mathbf{k}_{\mathrm{b}}; s) + 4\nu^2\omega_{\mathrm{b}}^2}\, ds, \tag{5.9}$$

where the path integral is taken along the full ray trajectory for the Raman light (the ray trajectory is parameterized by the path length s instead of time t, that has been used in Eqs. (5.3) and (5.4), where $\mathrm{d}s = v_{\mathrm{g}}\mathrm{d}t$ as this is a more natural parameterization for spatial growth). In the above, a_0 is the normalized vector potential $a_0 = eA/(m_{\mathrm{e}}c^2) \simeq 0.85\times10^{-9}\sqrt{I(\mathrm{W/cm^2})\lambda_0^2(\mu\mathrm{m})}$, where I is the pump light intensity evaluated at x(s),

$\mathbf{k}_\mathrm{b}$ is the spatial beat frequency between the incident and scattered light: $\mathbf{k}_\mathrm{b}(s) = \mathbf{k}_0(s) - \mathbf{k}_\mathrm{s}(s)$, ω_b is the (constant) beat frequency $\omega_\mathrm{b} = \omega_0 - \omega_\mathrm{s}$ and D_EPW is the EPW dispersion function that relates the mismatch between the beat frequency ω_b, of the two light waves, with the local frequency of a Langmuir wave:

$$D_\mathrm{EPW}(k_\mathrm{b}, \omega_\mathrm{b}) = \omega_\mathrm{b}^2 - [\omega_\mathrm{pe}^2(s) + 3v_\mathrm{e}^2 k_\mathrm{b}^2(s)]. \tag{5.10}$$

The incident light intensity $|a_0|^2[x(s)]$ and wavevector $\mathbf{k}_0[x(s)]$, along the path of the scattered light ray, are interpolated from the intensities and wavenumbers that are known at discrete points along the family of N incident light rays. The wavenumbers have been obtained from the solution to Eqs. (5.3) and (5.4), while the intensities are obtained by solving for the action conservation law along each incident ray. This equation is:

$$\frac{\mathrm{d}\log\mathcal{J}}{\mathrm{d}t} = -2c^2\frac{\partial^2\theta}{\partial x_\mathrm{m}\partial x_\mathrm{m}} - 2\nu_\mathrm{em}, \tag{5.11}$$

where $\mathcal{J} = 2\omega A^2$ is the wave action, A is the wave amplitude, $\nu_\mathrm{em} = 1/2(\omega_\mathrm{pe}^2/\omega^2)\nu_\mathrm{ei}$ is the amplitude (temporal) damping rate for EM waves, with $\nu_\mathrm{ei} \simeq 3\times10^{-6}\log\Lambda\, n_\mathrm{e} Z/T_\mathrm{e,eV}^{3/2}$ being the electron–ion collision frequency in inverse seconds [6]. ($\log\Lambda$ is the Coulomb logarithm, n_e is the electron density in cm^{-3}, Z is the ionization, and $T_\mathrm{e,eV}$ is the electron temperature in eV).

To solve Eq. (5.11) along each incident ray trajectory $\mathbf{x} = \mathbf{x}(t; x_0)$ the first term on the RHS of Eq. (5.11) (called the "focusing" tensor in Tracy *et al.* [12]) is required. This is quite straightforward to compute so long as a wave caustic is not encountered (the case here for densities below $n_\mathrm{c}/4$ where the intensity is required for the computation of SRS). This term represents the local divergence of rays $[\partial^2/(\partial x_\mathrm{m}\partial x_\mathrm{m})\theta \equiv \partial/\partial x_\mathrm{m} k_\mathrm{m}]$ and, as such, it only makes a significant contribution for densities above $n_\mathrm{c}/4$. It can be neglected in the SRS active region (roughly the area contained within the $n_\mathrm{e} = 0.1\, n_\mathrm{c}$ and $n_\mathrm{e} = 0.25\, n_\mathrm{c}$ isodensity contours in Fig. 5.4).

Pump depletion caused by SRS has also been ignored in Eq. (5.11) as have any effects of cross-beam energy transfer. The lack of pump depletion is consistent with the rather moderate SRS gain computed $O(10)$, while CBET is mostly confined to regions of higher density. As an aside, we recall that in a linearly varying plasma density profile of scale length L, Eq. (5.9) reproduces Rosenbluth gain [15, 16] for a straight line ray trajectory[2]:

$$G_{\mathrm{R}} = \frac{\pi k_{\mathrm{L}}^2 |a_0|^2 L}{4 k_{\mathrm{s}} \cos(\theta_\nabla)}. \tag{5.12}$$

It is refraction (bending of the scattered light ray trajectories) that regularizes the divergence in the Rosenbluth gain for sidescatter (angles $\theta \to \pm 90^\circ$). Note that the angle θ_∇ and the term "sidecatter" are defined with respect to the direction of the local density gradient.

5.4 Calculation results

Figure 5.5 shows the maximum gain of SRS light originating from beam B3 [Fig. 5.5a], and the corresponding detected wavelength [Fig. 5.5c], that falls within the angular acceptance of the SABS detector as a function of ray index and SRS angle. The highest gains observed reach $G \sim 15$ and are the result of a $\theta = -120^\circ$ scattering angle from ray 5 of beam B3. The rays are numbered 1-20, starting from the bottom (beam #3 is the lower of the two beams shown in Fig. 5.4. The SRS wavelength of this high gain ray, is $\lambda_{\mathrm{s}} \simeq (530 - 540)\,\mathrm{nm}$ which corresponds to a density of $n_{\mathrm{e}} \simeq 0.12\, n_{\mathrm{c}}$. This scattering condition is shown in Figure 5.6, with the lower panel of this figure showing a zoom-in of the scattering region. In the figure, several SRS scattering events are shown along ray 5 for a fixed scattering angle of θ = -120° and densities in the range $0.1 \lesssim n_e/n_c \lesssim 0.15$. It is evident that the Raman light (green rays) correspond to sidescatter with respect to the density gradient (about which the pump is obliquely incident). Furthermore, the sidescatter propagates backwards with

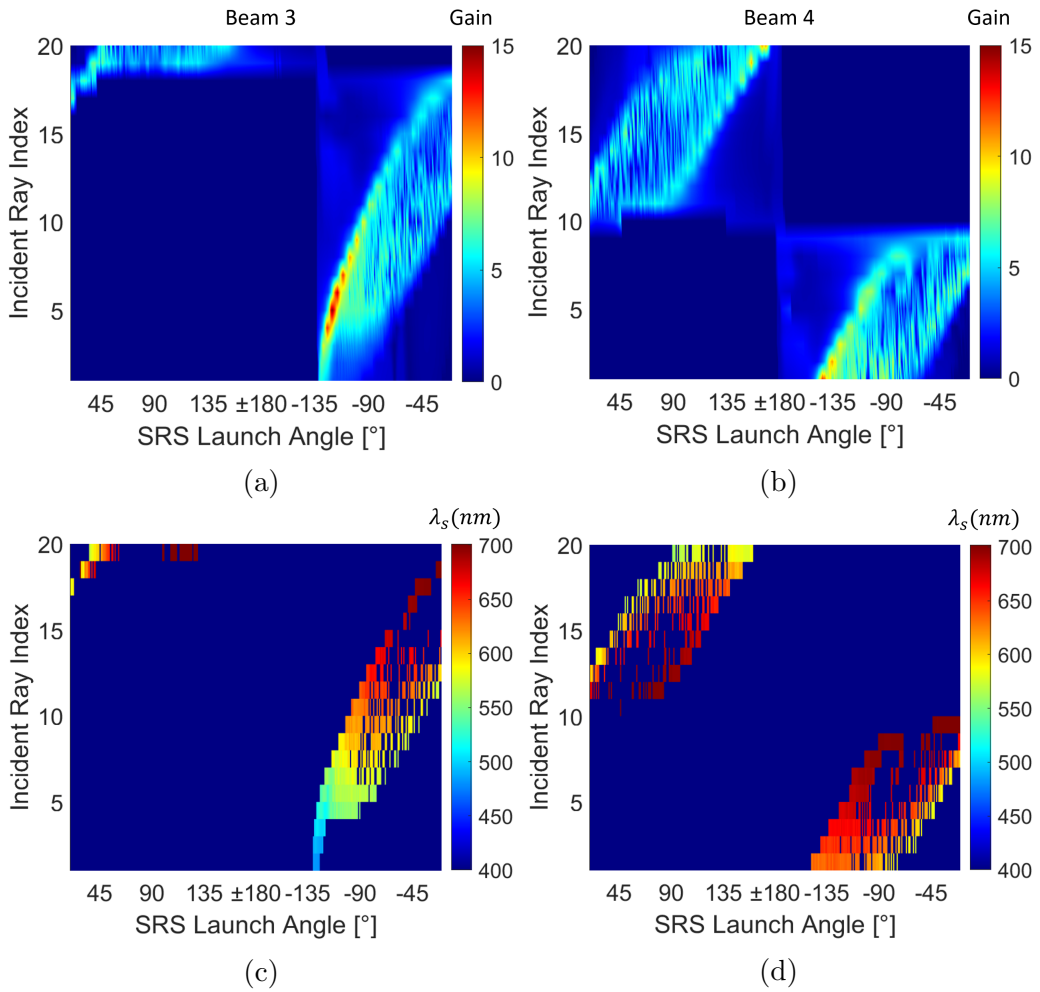

Figure 5.5: The maximum gain for detected SRS rays is shown as a function of local SRS angle (with respect to the incident light ray) and ray index for beams B3 (a) and B4 (b). Panels (c) and (d) show the SRS wavelength for the above.

respect to the pump. Notice that several conditions are responsible for this result: the scattering angle must compensate for refraction so that the SRS is detected, while only certain scattering angles will result in sidescatter and hence high gain. The considerations are responsible for the locus of maximum gain moving toward more forward scattering angles (and longer wavelength) as the selected rays move from the lower wing to the top: rays undergoing sidescatter near the center of the beam must occur at higher densities (longer wavelengths) in order to be detected (since more refraction is required).

The corresponding results for SRS originating from beam B4 (i.e., the beam con-

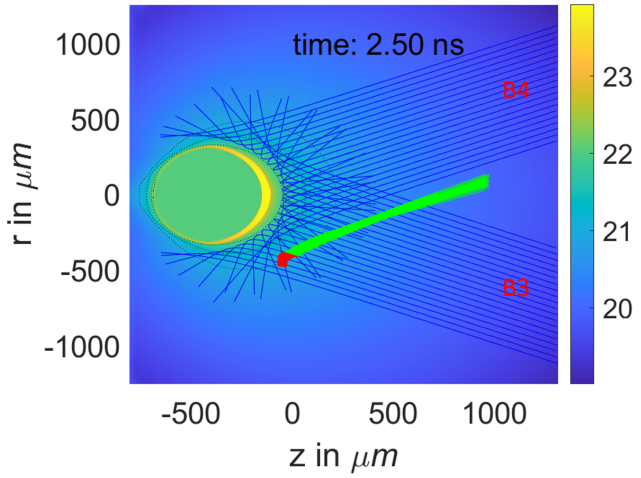

(a)

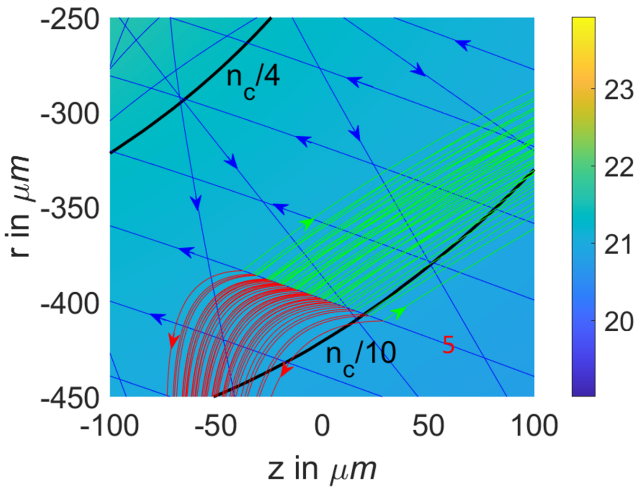

(b)

Figure 5.6: Sidescatter of the opposing beam (B3) can be observed in the SABS of beam B4. The incident light rays are marked with arrows and the isodensity contours are solid black lines.

taining SABS) are shown in Fig. 5.5b and Fig. 5.5d. The highest gain here ($G \simeq 12$) occurs for reasons similar to the highest gain rays from B3: It occurs for $\theta \simeq 150°$ scattering from ray #1 at a wavelength of approximately 650 nm this is a longer wavelength (higher density) than the highest gain ray originating from B3 because more refraction is required for detection. It is again sidescatter (Fig. 5.7). Scattering from the same ray can be detected for smaller scattering angles (down to $\lesssim 90°$ from the forward direction) but it must occur at a slightly lower density (shorter wavelength)

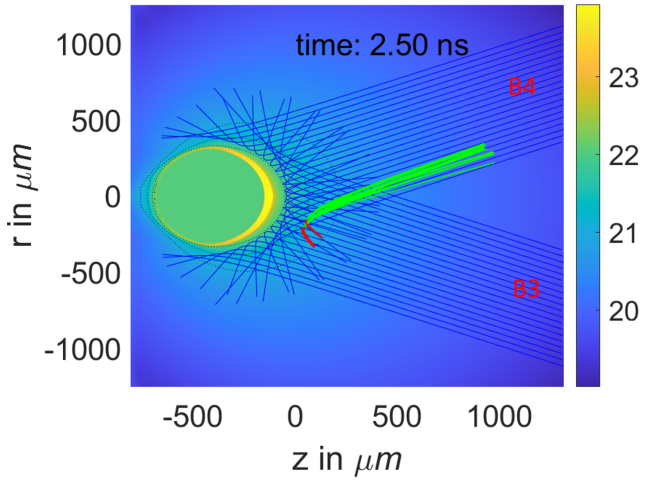

(a)

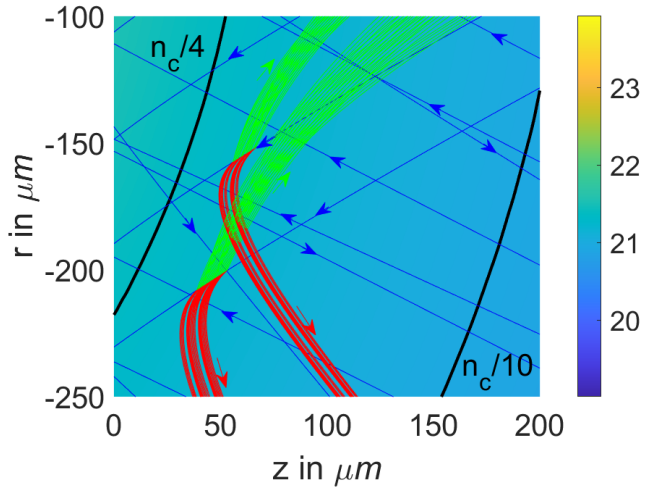

(b)

Figure 5.7: Sidescatter from the lower wing of beam B4 can be observed and has the highest gain. Raman events are shown for points sampled along rays 1 and 2.

to be detected and has lower gain because it is not sidescatter (Fig. 5.5d). As show in the zoom-in of this process [Fig. 5.7b], sidescatter at the position of ray #2 must occur at slightly higher density to be detected and at a more forward angle. This continues, with diminishing gain, until the center of the beam is reached (ray 10 in Fig. 5.5d). Moving to the upper wing of B4, the scattering angle must now move to the other side (downward direction) this accounts for the "jump" seen in Figs. 5.5b and 5.5c. Ray #11 (near the middle of B4) is $\theta \simeq 90°$, with Ray #20 (the upper wing) maximizing the gain for $\theta \simeq (160° - 170°)$. This is simultaneously near backscatter,

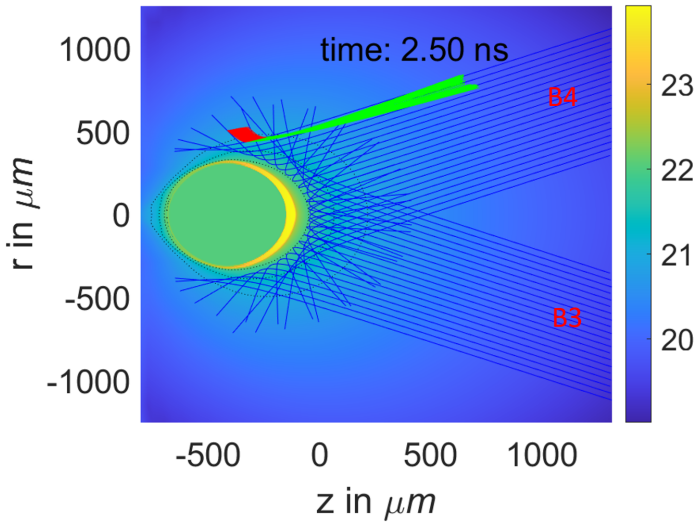

(a)

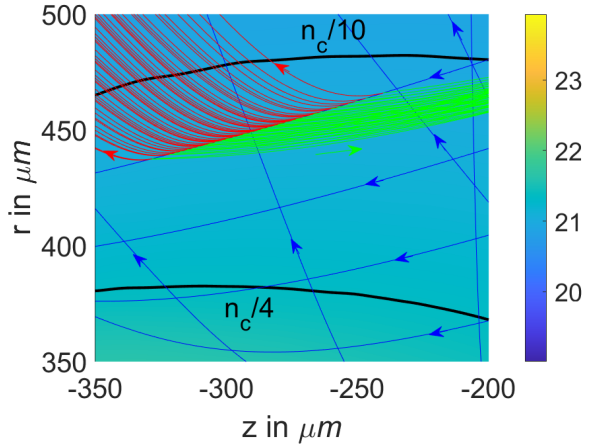

(b)

Figure 5.8: Sidescatter from the upper wing of beam B4 can be observed in its own lens. Raman events are shown sampled along the trajectory of ray #20. The high gain rays are sidescatter.

with respect to the pump, and sidescatter with respect to the density gradient (Fig. 5.8). The gain here is large ($G \sim 12$) and occurs at a scattered light wavelength of $\lambda_s \sim 580\,\text{nm}$. The maximum gains observed, irrespective of origin within a beam, as a function of scattered wavelength is shown in Fig. 5.9

It is seen that the mechanism of scattering is essentially the same for both beams, with each having similar peak gains. The peak gain from B3 is seen to occur at a shorter scattered wavelength than for B4 [Fig. 5.9]. The main result is that the

highest gains all correspond to sidescatter, with the gains for backscatter being small $G \sim 2$. The largest gains are also observed at the extremities/wings of the beam for B4 and to a lesser degree for B3. We speculate that the contribution from B4 could be decreased by the use of a smaller laser spot. In these experiments, the beam spots were quite large relative to the target size (750 μm spot versus 700 μm target diameter).

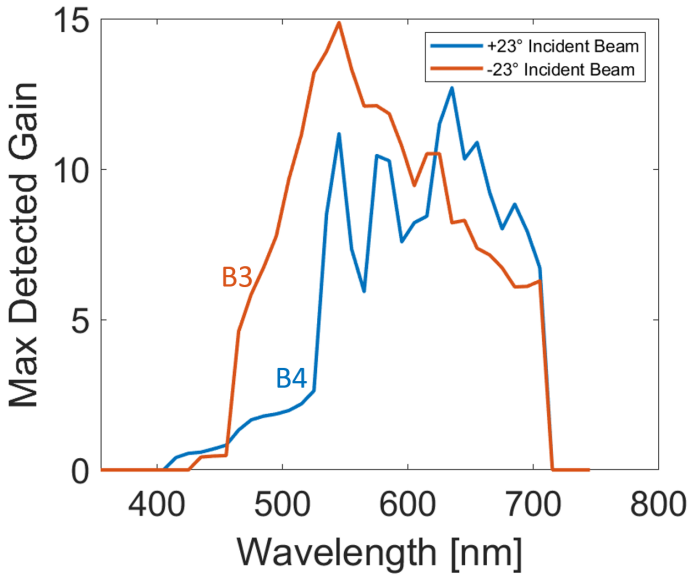

Figure 5.9: The maximum gain detected as a function of scattered light wavelength. The contributions from Beam 3 and 4 are plotted separately.

5.4.1 Comparison with experimental data

In comparing the predictions with experimental data, we see that several features are reproduced. However, care must be taken because only scattering events contained in plane "P" [Fig. 5.1] have been included.

Figure 5.10 shows that the brightest signal occurs at a scattered wavelength range $\lambda_s = (550 - 570)\,\mathrm{nm}$. This is in reasonable agreement with sidescatter from B3 [Fig. 5.9]. This is in reasonable agreement with sidescatter from beam B3 [Fig. 5.9] as the estimated gain at this wavelength is certainly sufficient to produce a strong scattered light signal. (Recall that our calculations correspond to t = 2.5 ns).

The model also predicts that substantial gain should be present over a wide range of scattered light wavelengths; the gain decreasing with increasing wavelength from beam 3 but somewhat less and more constant for beam 4. A decrease in scattered light signal is indeed observed with increasing wavelength (Fig. 5.10). However, our model is unable to capture the rapid drop in signal for $\lambda_s \gtrsim 640$ nm. This is the famous Raman gap, for which we currently have no explanation.

Figure 5.11 shows two experiments that can be used to isolate the contributions from beams B3 and B4. Unfortunately the long pass filter was present in these experiments. As a result, we are unable to conclusively determine that the brightest spectral feature [Fig. 5.10a] originates from beam B3. However we can conclude that beams B3 and B4 contribute about equally to scattered light of $\lambda_s \simeq 630$ nm, which is consistent with our predictions (Fig. 5.9).

5.5 Summary and discussion

Through the ray tracing analysis performed, based on predicted plasma profiles, we have shown that the main SRS mechanisms, active in OMEGA EP experiments, is most likely tangential sidescatter with respect to the local density gradient. This is because Raman light that is amplified in a direction perpendicular to the density gradient experiences a larger gain due to the weakest dephasing of the resonance by the density gradient.

We have demonstrated that the contributions from each incident beam to the detected SRS spectra is somewhat different with respect to its wavelength dependence. The shorter wavelength SRS being primarily generated from beam B3.

The good agreement between our simulations and the experimental results motivates future experiments without a long pass filter. This would permit an exploration of SRS with wavelengths in the range of $\sim$(500 - 600) nm, including an assessment of the relative contributions of beams B3 and B4. Future experiments might also investigate the polarization of the SRS.

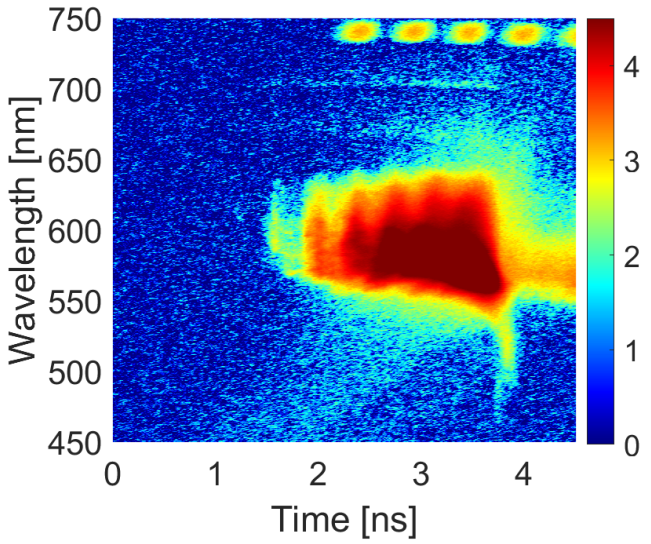

(a)

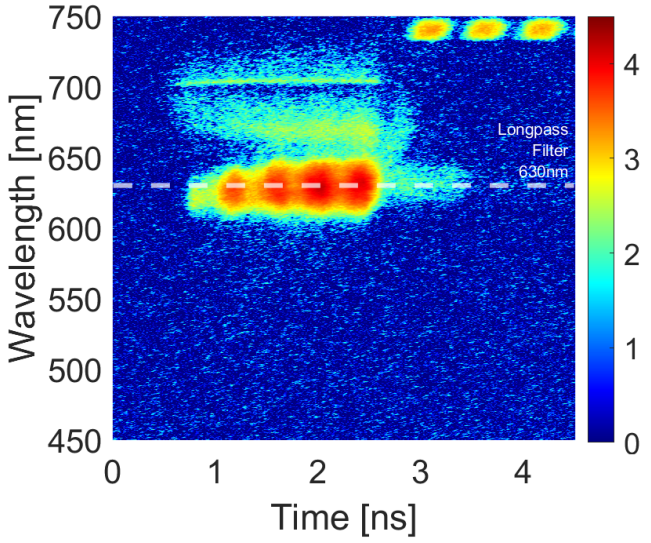

(b)

Figure 5.10: Time-resolved scattered light spectra for 4 ns ramp (shot # 30575) (a) and 2 ns square pulse with a long pass filter (shot # 30578) (b).

While we do see agreement within a wide range of wavelength, the shape of the SRS spectrum extends to shorter wavelength than the experimental data. We also provide no explanation for the "Raman gap". This could be due to inaccuracies in the hydrodynamic code predictions for the plasma profiles, or other factors that we have not accounted for in this work.

Future extensions to this work will include 3-D modeling and an investigation into

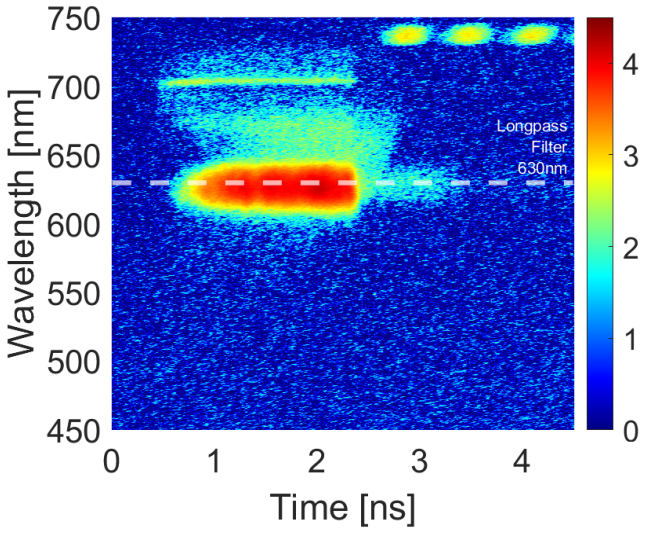

(a)

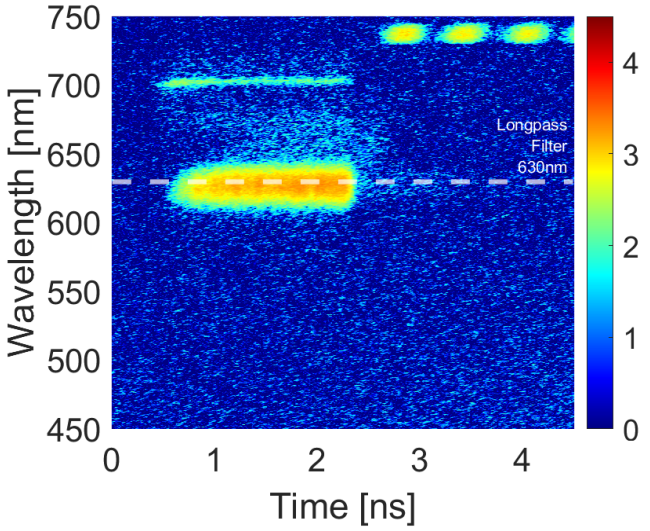

(b)

Figure 5.11: Streaked scattered light spectra for an experiment using beams B3 and B4 only (shot # 32063) (a); beam B4 only (shot # 32069) (b). The SABS diagnostic is within the aperture of beam 4 (Fig. 5.1).

the potential for sidescatter to become absolutely instable. The transition to absolute instability might provide an explanation for the existence of the Raman gap.

5.6 Acknowledgment

We acknowledges the support of the Natural Sciences and Engineering Research Council of Canada (NSERC), [funding reference numbers RGPIN-2018-05787, RGPAS-

2018-522497].

Cette recherche a été financée par le Conseil de recherches en sciences naturelles et en génie du Canada (CRSNG), [numéros de référence RGPIN-2018-05787, RGPAS-2018-522497].

This material is based upon work supported by the Department of Energy Nation Nuclear Security Administration under award Number DE-NA0001944, the University of Rochester, and the New York State Energy Research and Development Authority. The support of DOE does not constitute an endorsement by the DOE of the views expressed in this article.

References

[2] P. Michel, M. J. Rosenberg, W. Seka, A. A. Solodov, R. W. Short, T. Chapman, C. Goyon, N. Lemos, M. Hohenberger, J. D. Moody, S. P. Regan, and J. F. Myatt, "Theory and measurements of convective raman side scatter in inertial confinement fusion experiments," *Phys. Rev. E*, vol. 99, p. 033 203, 3 Mar. 2019. DOI: 10.1103/PhysRevE.99.033203. [Online]. Available: https://link.aps.org/doi/10.1103/PhysRevE.99.033203.

[6] W. L. Kruer, "The Physics of Laser Plasma Interactions," in, ser. Frontiers in Physics, D. Pines (Ed.) Vol. 73, Redwood City, CA: Addison-Wesley, 1988.

[7] M. J. Rosenberg, A. A. Solodov, J. F. Myatt, S. Hironaka, R. K. Follett, T. Filkins, A. V. Maximov, C. Ren, S. Cao, P. Michel, W. Seka, M. S. Wei, M. Hohenberger, J. P. Palastro, R. H. H. Scott, K. Glize, and S. P. Regan, "Effect of overlapping laser beams and density scale length in laser-plasma instability experiments on omega ep (**in preparation**)," *Phys. Plasmas*, 2021.

[12] E. R. Tracy, A. J. Brizard, A. S. Richardson, and A. N. Kaufman, *Ray Tracing and Beyond*. Cambridge, United Kingdom: Cambridge University Press, 2014.

[13] P. B. Radha, V. N. Goncharov, T. J. B. Collins, J. A. Delettrez, Y. Elbaz, V. Y. Glebov, R. L. Keck, D. E. Keller, J. P. Knauer, and J. A. Marozas, "Multidimensional analysis of direct-drive, plastic-shell implosions on OMEGA," *Phys. Plasmas*, vol. 12, 056307, 2005. DOI: http://dx.doi.org/10.1063/1.1882333. [Online]. Available: http://scitation.aip.org/content/aip/journal/pop/12/5/10.1063/1.1882333.

[14] M. J. Rosenberg, A. A. Solodov, W. Seka, R. K. Follett, J. F. Myatt, A. V. Maximov, C. Ren, S. Cao, P. Michel, M. Hohenberger, J. P. Palastro, C. Goyon, T. Chapman, J. E. Ralph, J. D. Moody, R. H. H. Scott, K. Glize, and S. P. Regan, "Stimulated raman scattering mechanisms and scaling behavior in planar direct-drive experiments at the national ignition facility," *Physics of Plasmas*, vol. 27, no. 4, p. 042 705, 2020. [Online]. Available: https://doi.org/10.1063/1.5139226.

[15] M. N. Rosenbluth, "Parametric instabilities in inhomogeneous media," *Phys. Rev. Lett.*, vol. 29, pp. 565–567, 9 Aug. 1972. DOI: 10.1103/PhysRevLett.29.565. [Online]. Available: https://link.aps.org/doi/10.1103/PhysRevLett.29.565.

[16] D. Pesme, G. Laval, and R. Pellat, "Parametric instabilities in bounded plasmas," *Phys. Rev. Lett.*, vol. 31, pp. 203–206, 4 Jul. 1973. DOI: 10.1103/PhysRevLett.31.203. [Online]. Available: https://link.aps.org/doi/10.1103/PhysRevLett.31.203.

Chapter 6

Conclusions, Recommendations, & Future Work

6.1 Conclusions

In the work presented in this thesis, a ray tracing approach was taken in the Eikonal Laser Plasma Simulation Environment (ELPSE) to predict the stimulated Raman scattered (SRS) light spectra in spherical target experiments done on the OMEGA EP laser. Recent experiments conducted at the Nation Ignition Facility suggest that SRS sidescatter (with respect to the density gradient) is possibly responsible for the observed hot electron generation[1, 2]. This work was motivated by the fact that SRS sidescatter can generate hot electrons is a concern for directly-driven inertial confinement fusion.

The ray tracing model we developed is able to predict the time-dependent scattered light spectra from experiments done on OMEGA EP. The model can also identify the origins of high gain Raman light, as well as which SRS mechanisms create the most high gain Raman light. We see that the mechanism that creates the largest gain is tangential sidescatter. Tangential sidescatter is where the scattered light is launched near parallel to isodensity contours. When the scattered light travels through near resonant densities it accumulates a large gain, as seen from the path integral gain formula derived by Michel *et al.* [2]. In this work, we calculated the gain of Raman rays that hit the detector and therefore only observed tangential sidescatter that

would refract towards the detector. The comparison of the scattered light spectra and the experimental data was favourable.

6.2 Future Work

The ray tracing analysis of stimulated Raman scattering in spherical target experiments on OMEGA EP motivates further experiments on EP to further explore SRS mitigation strategies. The simulation results show a large amount of SRS with $\lambda_s \lesssim$ 630 nm. This motivates experiments to be done on OMEGA EP where SABS does not have the long pass filter applied.

As the ray tracing code stands, it could be utilised to predict Thomson scattering off of the electron plasma waves that can be propagated in the simulation. In the simulations done for the work presented in this paper, the incident beam intensity was taken to be constant over all incident beam rays. Further use of this simulation code could implement varying ray intensities across the beam to more accurately predict the SRS spectra. This code also only calculates the gain of Raman light rays that hit the detector. It could be interesting to further investigate the physics of SRS gain instead of just trying to predict the detected scattered light spectra.

The simulation code should eventually be converted into a three-dimensional code for further understanding of OMEGA EP experiments. Adding more resolution (i.e, increase the number of incident rays per beam and increase the sampling done) would increase the accuracy. In this work we focus on the highest gain detected per wavelength band ($\sim$ 10 nm), however, developing a way to instead look at the overall detected intensity on the SRS spectra would be a better comparison to the experimental data. However, all three of these suggestions would greatly increase the computation time.

References

[1] M. J. Rosenberg, A. A. Solodov, J. F. Myatt, W. Seka, P. Michel, M. Hohenberger, R. W. Short, R. Epstein, S. P. Regan, E. M. Campbell, T. Chapman, C. Goyon, J. E. Ralph, M. A. Barrios, J. D. Moody, and J. W. Bates, "Origins and scaling of hot-electron preheat in ignition-scale direct-drive inertial confinement fusion experiments," *Phys. Rev. Lett.*, vol. 120, p. 055 001, 5 Jan. 2018. DOI: 10.1103/PhysRevLett.120.055001. [Online]. Available: https://link.aps.org/doi/10.1103/PhysRevLett.120.055001.

[2] P. Michel, M. J. Rosenberg, W. Seka, A. A. Solodov, R. W. Short, T. Chapman, C. Goyon, N. Lemos, M. Hohenberger, J. D. Moody, S. P. Regan, and J. F. Myatt, "Theory and measurements of convective raman side scatter in inertial confinement fusion experiments," *Phys. Rev. E*, vol. 99, p. 033 203, 3 Mar. 2019. DOI: 10.1103/PhysRevE.99.033203. [Online]. Available: https://link.aps.org/doi/10.1103/PhysRevE.99.033203.

Bibliography

[1] M. J. Rosenberg, A. A. Solodov, J. F. Myatt, W. Seka, P. Michel, M. Hohenberger, R. W. Short, R. Epstein, S. P. Regan, E. M. Campbell, T. Chapman, C. Goyon, J. E. Ralph, M. A. Barrios, J. D. Moody, and J. W. Bates, "Origins and scaling of hot-electron preheat in ignition-scale direct-drive inertial confinement fusion experiments," *Phys. Rev. Lett.*, vol. 120, p. 055 001, 5 Jan. 2018. DOI: 10.1103/PhysRevLett.120.055001. [Online]. Available: https://link.aps.org/doi/10.1103/PhysRevLett.120.055001.

[2] P. Michel, M. J. Rosenberg, W. Seka, A. A. Solodov, R. W. Short, T. Chapman, C. Goyon, N. Lemos, M. Hohenberger, J. D. Moody, S. P. Regan, and J. F. Myatt, "Theory and measurements of convective raman side scatter in inertial confinement fusion experiments," *Phys. Rev. E*, vol. 99, p. 033 203, 3 Mar. 2019. DOI: 10.1103/PhysRevE.99.033203. [Online]. Available: https://link.aps.org/doi/10.1103/PhysRevE.99.033203.

[3] J. Nuckolls, L. Wood, and A. Thiessen, "Laser compression of matter to super-high densities: Thermonuclear (ctr) applications," vol. 239, 1972. DOI: 10.1038/239139a0.

[4] J. Lindl, "Development of indirect-drive approach to inertial confinement fusion and the target physics basis for ignition and gain," *Physics of Plasmas*, vol. 2, 1995. DOI: 10.1063/1.871025.

[5] R. S. Craxton, K. S. Anderson, T. R. Boehly, V. N. Goncharov, D. R. Harding, J. P. Knauer, R. L. McCrory, P. W. McKenty, D. D. Meyerhofer, J. F. Myatt, A. J. Schmitt, J. D. Sethian, R. W. Short, S. Skupsky, W. Theobald, W. L. Kruer, K. Tanaka, R. Betti, T. J. B. Collins, J. A. Delettrez, S. X. Hu, J. A. Marozas, A. V. Maximov, D. T. Michel, P. B. Radha, S. P. Regan, T. C. Sangster, W. Seka, A. A. Solodov, J. M. Soures, C. Stoeckl, and J. D. Zuegel, "Direct-drive inertial confinement fusion: A review," *Phys. Plasmas*, vol. 22, no. 11, p. 110 501, 2015. DOI: 10.1063/1.4934714.

[6] W. L. Kruer, "The Physics of Laser Plasma Interactions," in, ser. Frontiers in Physics, D. Pines (Ed.) Vol. 73, Redwood City, CA: Addison-Wesley, 1988.

[7] M. J. Rosenberg, A. A. Solodov, J. F. Myatt, S. Hironaka, R. K. Follett, T. Filkins, A. V. Maximov, C. Ren, S. Cao, P. Michel, W. Seka, M. S. Wei, M. Hohenberger, J. P. Palastro, R. H. H. Scott, K. Glize, and S. P. Regan, "Effect of overlapping laser beams and density scale length in laser-plasma instability experiments on omega ep (**in preparation**)," *Phys. Plasmas*, 2021.

[8] R. W. Boyd, *Nonlinear Optics, Third Edition*, 3rd. USA: Academic Press, Inc., 2008, ISBN: 0123694701.

[9] D. E. Hinkel, M. D. Rosen, E. A. Williams, A. B. Langdon, C. H. Still, D. A. Callahan, J. D. Moody, P. A. Michel, R. P. J. Town, R. A. London, and S. H. Langer, "Stimulated raman scatter analyses of experiments conducted at the national ignition facility," *Phys. Plasmas*, vol. 18, p. 056 312, 2011.

[10] J. Heading, "An introduction to phase-integral methods," 1962.

[11] C. P. H. Goldstein and J. Safko, *Classical Mechanics*, 3rd. Pearson, 2002.

[12] E. R. Tracy, A. J. Brizard, A. S. Richardson, and A. N. Kaufman, *Ray Tracing and Beyond*. Cambridge, United Kingdom: Cambridge University Press, 2014.

[13] P. B. Radha, V. N. Goncharov, T. J. B. Collins, J. A. Delettrez, Y. Elbaz, V. Y. Glebov, R. L. Keck, D. E. Keller, J. P. Knauer, and J. A. Marozas, "Multidimensional analysis of direct-drive, plastic-shell implosions on OMEGA," *Phys. Plasmas*, vol. 12, 056307, 2005. DOI: http://dx.doi.org/10.1063/1.1882333. [Online]. Available: http://scitation.aip.org/content/aip/journal/pop/12/5/10.1063/1.1882333.

[14] M. J. Rosenberg, A. A. Solodov, W. Seka, R. K. Follett, J. F. Myatt, A. V. Maximov, C. Ren, S. Cao, P. Michel, M. Hohenberger, J. P. Palastro, C. Goyon, T. Chapman, J. E. Ralph, J. D. Moody, R. H. H. Scott, K. Glize, and S. P. Regan, "Stimulated raman scattering mechanisms and scaling behavior in planar direct-drive experiments at the national ignition facility," *Physics of Plasmas*, vol. 27, no. 4, p. 042 705, 2020. [Online]. Available: https://doi.org/10.1063/1.5139226.

[15] M. N. Rosenbluth, "Parametric instabilities in inhomogeneous media," *Phys. Rev. Lett.*, vol. 29, pp. 565–567, 9 Aug. 1972. DOI: 10.1103/PhysRevLett.29.565. [Online]. Available: https://link.aps.org/doi/10.1103/PhysRevLett.29.565.

[16] D. Pesme, G. Laval, and R. Pellat, "Parametric instabilities in bounded plasmas," *Phys. Rev. Lett.*, vol. 31, pp. 203–206, 4 Jul. 1973. DOI: 10.1103/PhysRevLett.31.203. [Online]. Available: https://link.aps.org/doi/10.1103/PhysRevLett.31.203.